Article

SOURCE DATA | TRANSPARENT PROCESS | OPEN ACCESS | CHECK FOR UPDATES

THE EMBO JOURNAL

A conserved basic motif mediates membrane anchoring and TRAF2 recruitment across costimulatory TNFRs

Jiali Zhu [1,6], Xi Xu [1,6], Pei Liu[1], Hui Wu[1], Yuxuan Wang[1], Boying Xu[2], Maorong Wen[3], Min Chen[4], Zhifeng Chen [1]✉, James J Chou [4,5]✉ & Linlin Zhao [1]✉

Abstract

Costimulatory receptors of the TNFR superfamily are key components in synthetic immunoreceptors, yet how their intracellular domains coordinate membrane anchoring with adaptor recruitment remains unresolved. Here, using solution-state NMR and membrane-reconstituted FRET assays, we identify a conserved basic-residue-rich sequence (BRS) in the juxtamembrane region of OX40 that binds anionic phospholipids and adopts a membrane-inserted conformation. This membrane engagement enables a dual-site interaction with TRAF2, combining canonical PxQxx binding with a secondary membrane-proximal interface, to promote robust NF-κB activation. Disruption of the BRS impairs adaptor docking without reducing receptor surface expression or ligand-induced clustering. This regulatory architecture is further supported in 4-1BB and CD40, indicating broader relevance across TNFR costimulatory receptors. Our findings refine current models of TNFR signaling and offer a generalizable framework for receptor design. Incorporating membrane-anchoring motifs into synthetic constructs may enhance spatial control of adaptor recruitment, thereby improving signal fidelity, sensitivity, and performance in CAR-T applications.

Subject Categories Immunology; Signal Transduction; Structural Biology
https://doi.org/10.1038/s44318-026-00868-z
Received 4 December 2025; Revised 7 July 2026;
Accepted 8 July 2026
Published online: 15 July 2026

Introduction

Members of the tumor necrosis factor receptor (TNFR) superfamily are essential regulators of T cell activation and function (Chen and Flies, 2013; Croft, 2003; Morris and Allen, 2012). Their cytoplasmic domains (CTD), which engage adaptor proteins such as TRAFs to initiate downstream signaling, have been widely incorporated into chimeric antigen receptor (CAR) designs to enhance CAR-T cell persistence, expansion, and cytotoxicity (Jaeger-Ruckstuhl et al, 2024; Larson and Maus, 2021; Mackensen et al, 2022; Wehrli and Maus, 2021). Among these, OX40 (CD134) has emerged as a key costimulatory module, with its CTD shown to promote cytokine production and long-term memory formation (Katsarou et al, 2021; Tan et al, 2022; Zhang et al, 2021; Zhang et al, 2025). However, despite its growing application, the spatial and regulatory mechanisms underlying OX40 mediated signaling remain poorly defined, limiting its rational optimization in CAR engineering (Edner et al, 2020; Renand et al, 2020; Wang et al, 2024).

The cytoplasmic domain (CTD) of OX40 transduces signals primarily through the recruitment of TRAF adaptor proteins (Kawamata et al, 1998; Thapa et al, 2024; Xiao et al, 2012). Structural analyses of several TNFR costimulatory receptors have established that a conserved PxQxx motif, located at the C-terminus of their CTD, mediates binding to TRAF2, TRAF3, and TRAF5 (Compaan and Hymowitz, 2006; Croft, 2009, 2010). While this canonical motif in the ~40 amino acid CTD of OX40 has been extensively characterized and integrated into CAR-T designs, the functional significance of other regions, particularly the membrane-proximal segment, remains unresolved.

Sequence alignment revealed that the juxtamembrane region of OX40 is enriched in conserved basic residues, including R241, R242, R245, and K252, forming a basic residue rich sequence (BRS) immediately downstream of the transmembrane domain. This motif suggests a potential regulatory role. Previous studies have shown that similar basic clusters mediate membrane association and conformational regulation in other immune receptors. In CD28 and CD3ε, such residues facilitate membrane insertion of ITAM elements, modulating activation thresholds (Jiang et al, 2025; Xu et al, 2008; Yang et al, 2017). In PD-L1, basic residues contribute to membrane retention by shielding ubiquitination sites, thereby enhancing surface stability (Wen et al, 2021). These observations indicate that BRS motifs may serve as structural elements critical for spatial organization and signal integration of membrane receptors (Harayama and Riezman, 2018; Wang et al, 2014).

Building on the above analyses, this study systematically investigates the functional role of the OX40 intracellular domain,

[1]Department of Anesthesiology, Putuo People's Hospital, School of Medicine, Tongji University, Shanghai, China. [2]Tongji University Cancer Center, Shanghai Tenth People's Hospital, School of Medicine, Tongji University, Shanghai, China. [3]Hangzhou Weizhi Biotechnology Co., Ltd, Hangzhou, China. [4]Interdisciplinary Research Center on Biology and Chemistry, Shanghai Institute of Organic Chemistry, Chinese Academy of Sciences, Shanghai, China. [5]State Key Laboratory of Chemical Biology, Shanghai Institute of Organic Chemistry, Chinese Academy of Sciences, Shanghai, China. [6]These authors contributed equally: Jiali Zhu, Xi Xu. ✉E-mail: 2305635@tongji.edu.cn; james_chou@mail.sioc.ac.cn; lzhao@tongji.edu.cn

© The Author(s)

with particular focus on the membrane-proximal basic residue rich sequence (BRS) and its contribution to membrane anchoring and signal transduction. Structural and functional analyses revealed that the conserved arginine residues R241 and R242 mediate specific recognition of negatively charged phospholipids on the inner leaflet of the plasma membrane, stabilizing a membrane anchored conformation of residues 236–242. This BRS motif contributes to formation of a membrane-proximal interface with the C-terminal domain of TRAF2, enabling its membrane localized recruitment and promoting formation of a membrane-proximal OX40-TRAF2 complex essential for NF-κB activation. Mutagenesis of R241 and R242 to neutral residues markedly impaired phospholipid binding and TRAF2 association, resulting in an almost complete loss of downstream signaling. Extending this mechanism to other TNFR family costimulatory receptors, including 4-1BB and CD40, revealed that conserved basic residues within their juxtamembrane regions similarly support TRAF-mediated NF-κB activation, indicating that BRS dependent membrane anchoring represents a broadly conserved signaling strategy within the TNFR superfamily.

This work delineates a previously unrecognized mechanism by which the OX40 BRS coordinates membrane lipid engagement and TRAF2 docking to facilitate signal initiation (Ye et al, 1999). These findings identify the BRS as a second, functionally distinct signaling interface that cooperates with the canonical C-terminal PxQxx TRAF-binding motif, thereby expanding the current model of TNFR signal integration (Ceccarelli et al, 2017). This conceptual advance provides a mechanistic framework for the rational design of OX40 targeting biologics and CAR-T constructs, emphasizing the necessity of incorporating both canonical and membrane anchoring motifs for effective immune modulation.

Results

OX40 juxtamembrane domain interactions with anionic phospholipids

Cellular membranes exhibit distinct phospholipid compositions, with intracellular membranes being particularly enriched in anionic phospholipids such as phosphatidylserine (PS), phosphatidylinositol (PI), and phosphatidylglycerol (PG) (Harayama and Riezman, 2018). These negatively charged lipids play pivotal roles in stabilizing membrane receptors and orchestrating signal transduction cascades (Singh et al, 2024; Skotland and Sandvig, 2019; Wang et al, 2014; Yen et al, 2018). Sequence analysis revealed that the intracellular juxtamembrane domain of OX40 contains evolutionarily conserved basic residue arginine (R241/R242) and a polar tyrosine (Y238) with elevated pKa (Appendix Fig. S1A). To investigate potential lipid-protein interactions, we expressed recombinant peptides spanning OX40 residues 236–277, encompassing both juxtamembrane and cytosolic regions, purified in *E.coli* to >95% homogeneity, and validated by MALDI-TOF mass spectrometry (Appendix Fig. S1B–D).

Uniformly $^{15}N/^{13}C$-labeled $OX40_{236\text{-}277}$ samples were analyzed using solution-state NMR spectroscopy, yielding complete backbone assignments, except for four proline residues (P247, P248, P253, P254) (Fig. 1A). To simulate T cell membrane environments, bicelle systems ($q = 0.8$) containing either zwitterionic DMPC or anionic DMPG were titrated into the NMR samples. Notably, significant chemical shift perturbations (CSPs) were observed exclusively upon titration with DMPG bicelles, whereas no CSPs were detected with DMPC bicelles (Fig. 1B; Appendix Fig. S1E). Mapping of the DMPG-induced CSPs revealed a critical interaction hotspot spanning residues 236–242, a structurally conserved linker that bridges the transmembrane helix and the cytoplasmic signaling loops. This region, which includes three polar residues (Y238, R241, R242), is likely involved in mediating electrostatic interactions. To dissect residue specific contributions, alanine or serine substitutions were introduced: Y238A (Y-A), R241S/R242S (2R-S), and the triple mutant Y238A/R241S/R242S. CSP analysis of the remaining residues (A236, L237, L239, L240) during DMPG titration revealed that the R241/R242 mutations significantly attenuated lipid-induced perturbations, while Y238A resulted in moderate effects. Complete abolition of CSPs in the triple mutant confirmed the cooperative engagement of these residues (Fig. 1C; Appendix Fig. S2A–D).

We then conducted paramagnetic relaxation enhancement (PRE) experiments using 16-doxylstearic acid (16-DSA) to provide direct evidence of membrane partitioning. $OX40_{236\text{-}277}$ exhibited pronounced PRE effects at residues 236–242 upon DMPG incorporation, such as Y238/L240, indicating deep insertion of the N-terminal juxtamembrane segment into the lipid bilayer. In contrast, minimal PRE amplitudes at the C-terminus confirmed aqueous exposure, such as T261/L274, establishing a clear boundary between the membrane embedded and cytosolic domains (Fig. 1D; Appendix Fig. S2E). Overall, we conclude that the juxtamembrane domain of OX40 specifically interacts with negatively charged phospholipids, primarily mediated by two conserved arginine residues.

Membrane embedded dynamics of the OX40 236–242 motif

To corroborate the membrane partitioning mechanism, we performed deuterium decoupled nuclear Overhauser effect (NOE) spectroscopy on perdeuterated $OX40_{236\text{-}277}$ samples reconstituted in DMPG bicelles ($q = 0.8$). Strategic deuteration of both the protein amide and alkyl groups or DH6PC eliminated spurious background signals, enabling unambiguous detection of lipid-protein interactions. Striking NOE correlations (< 5 Å) were observed between the acyl chains of DMPG and six consecutive residues (A236-R241), supporting insertion into, or close proximity to, the lipid acyl chain region (Fig. 2A). While R242 exhibited attenuated NOE signals due to intrinsic spectral broadening, neighboring residue R245, despite its solvent exposed location and strong backbone amide intensity, showed no detectable lipid contacts, excluding nonspecific electrostatic interactions.

To complement NMR findings, we established a fluorescence resonance energy transfer (FRET) assay probing real time membrane insertion dynamics. NHS-rhodamine labeled $OX40_{236\text{-}277}$ (randomly conjugated to primary amines and lysine side chains) was reconstituted in DMPG liposome containing ~10% NBD-PE as FRET donor. Upon 463 nm excitation, wild-type (WT) samples exhibited strong emission at 593 nm (FRET efficiency = 0.55 ± 0.05), indicative of close proximity between the 236 and 242 motif and lipid acyl chains (Fig. 2B,C). Mutation of juxtamembrane arginine residues (R241S/R242S) reduced FRET efficiency by 25%, whereas Y238A showed no significant attenuation. This dichotomy

 © The Author(s)

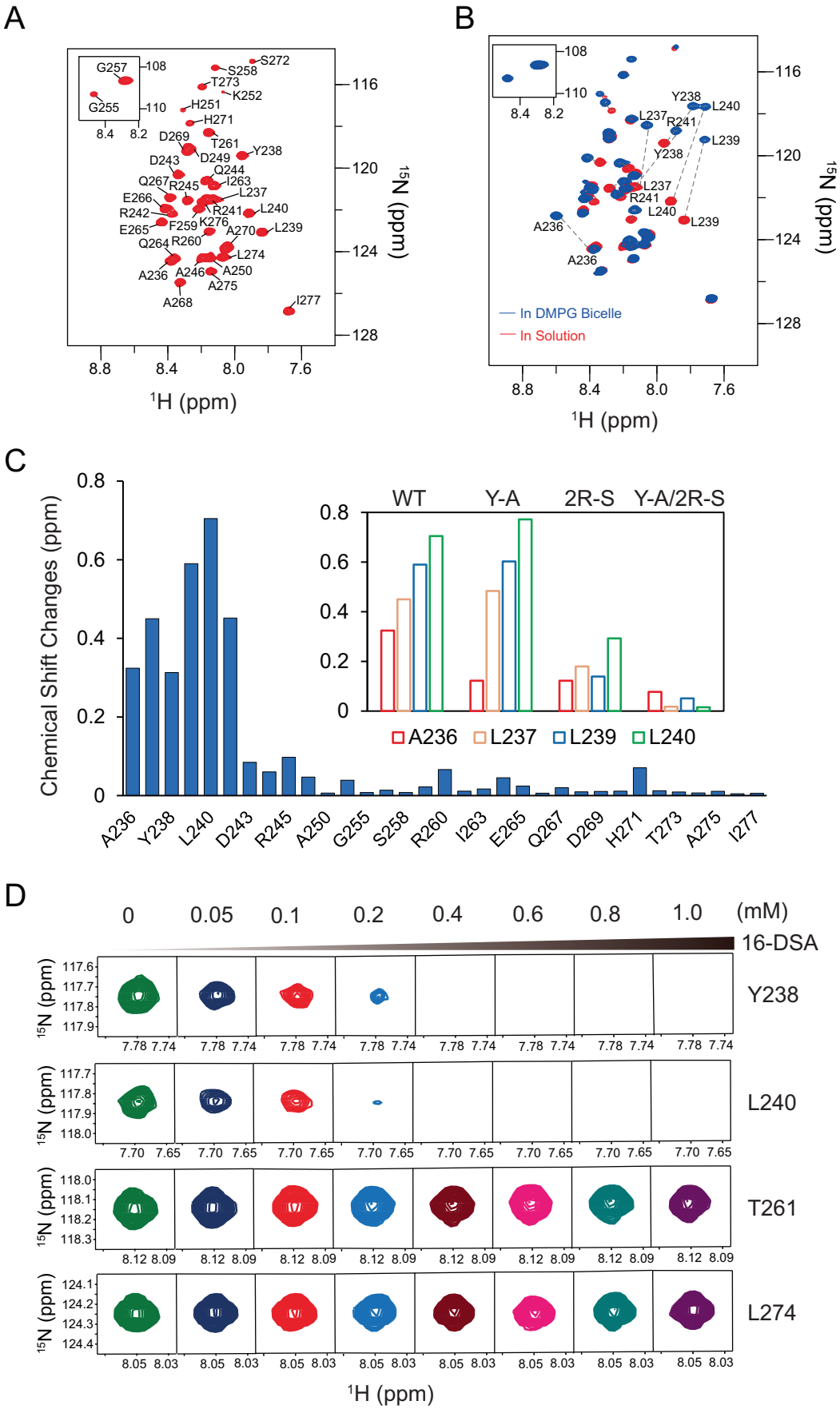

A
B
C
D
In DMPG Bicelle
In Solution
WT
Y-A
2R-S
Y-A/2R-S
A236
L237
L239
L240
Chemical Shift Changes (ppm)
16-DSA
(mM)
0
0.05
0.1
0.2
0.4
0.6
0.8
1.0
Y238
L240
T261
L274
^{1}H (ppm)
^{15}N (ppm)

Figure 1. The OX40 juxtamembrane domain engages anionic phospholipids through conserved arginine residues.

(**A**) Backbone resonance assignments of the OX40 juxtamembrane and intracellular domains (residues 236–277) in aqueous solution. (**B**) Chemical shift perturbations (CSPs) of $OX40_{236-277}$ in aqueous solution (red) versus DMPG bicelles (blue) at 1:65 molar ratio (OX40: DMPG). Dashed arrows indicate residues with CSP > 0.2 ppm. Bicelles were prepared with $q = 0.8$ (DMPG/DH_6PC). (**C**) Quantitative analysis of DMPG-induced CSPs. Upper inset shows residual CSPs for residues A236/L237/L239/L240 in Y238A, R241S/R242S or triple mutant, corresponding with data in Appendix Fig. S2A–D. (**D**) Paramagnetic relaxation enhancement (PRE) effects on $OX40_{236-277}$ in DMPG bicelles titrated with 16-DSA (0–1.0 mM in 7 steps). Signal attenuation profiles reflect membrane proximity of specific residues (correlative data in Appendix Fig. S2E). Source data are available online for this figure.

suggests R241/R242 mediate electrostatic membrane docking. Introducing additional mutations (Y238A/R241S/R242S/R245S) shows no FRET signals difference with R241S/R242S, confirming cooperative engagement of the entire 236–242 cassette in membrane partitioning.

Complementary relaxation analyses (T1, T2, heteronuclear NOE) revealed profound dynamic restructuring upon lipid binding. The 236–242 motif exhibited a fivefold increase in R2 (20.6 s^{-1} in DMPG bicelle vs. 3.2 s^{-1} in solution) and elevated heteronuclear NOE values (0.52 vs. 0.12), indicating transition to a conformationally rigid state characteristic of membrane-anchored domains (Fig. 2D). These collective data establish that anionic phospholipids stabilize the juxtamembrane region through both electrostatic attraction and hydrophobic burial.

By integrating NMR spectroscopy with in vitro FRET assays, we identified R241 and R242 as critical determinants of membrane partitioning within the OX40 juxtamembrane domain. These evolutionarily conserved arginine residues facilitate dual stabilization through two mechanisms: electrostatic steering via coordination with anionic phospholipid headgroups, and hydrophobic insertion mediated by adjacent aliphatic residues (A236, L237, L239, L240).

R241/R242 driven membrane anchoring enhances NF-κB signaling without reducing receptor surface expression or ligand-induced clustering

Juxtamembrane basic residue rich sequences (BRS) have been shown to play critical roles in various membrane proteins, contributing either to receptor stability, as observed in PD-L1 (Wen et al, 2021), or to downstream signaling, as in CD3ε (Xu et al, 2008). Given the importance of arginine residues R241 and R242 in anchoring the 236–242 motif of OX40 to the membrane, we further investigated whether this localization affects receptor turnover or signaling efficacy in a cellular context.

To evaluate receptor turnover, we performed cycloheximide (CHX) chase assays in two independent T-cell-derived systems. WT OX40 or the R241S, R242S and R241S/R242S double mutant (2R-S) were stably expressed in Jurkat cells, which have low basal OX40 expression, and in HuT78 sgOX40 cells, in which endogenous OX40 was depleted and reconstituted with the corresponding WT or mutant receptors (Appendix Fig. S3A–C). After blockade of protein synthesis with CHX, Flag-OX40 levels were monitored over time by immunoblotting and normalized to tubulin (Fig. 3A–D). In both Jurkat and HuT78 sgOX40 reconstituted cells, the BRS mutants showed slower loss of Flag-OX40 than WT OX40, with the 2R-S mutant displaying the most delayed turnover. Thus, mutation of R241/R242 does not destabilize OX40 or accelerate receptor degradation. Instead, BRS mutation delays OX40 turnover in T-cell-derived systems.

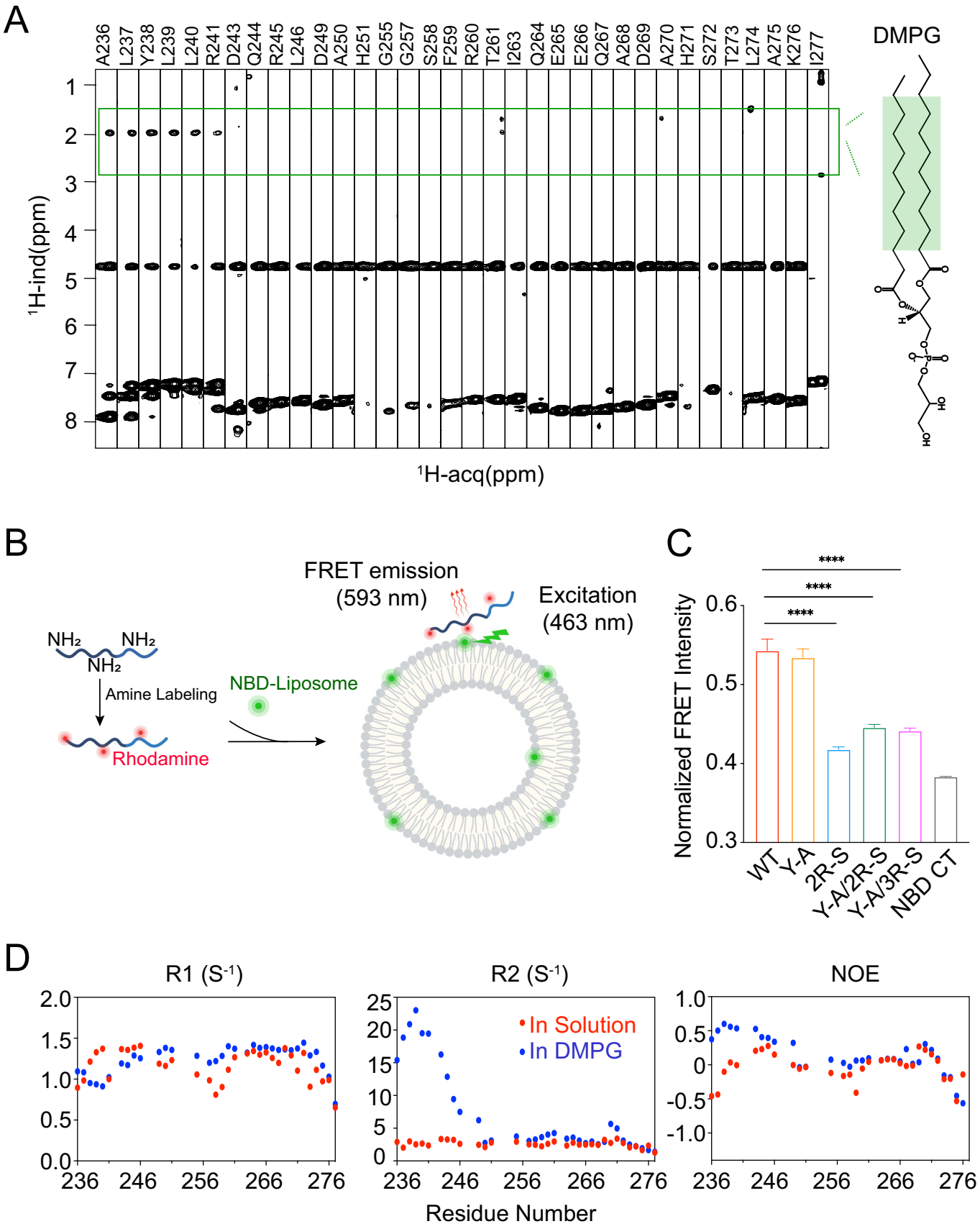
We next examined whether the mutations affect OX40 oligomerization at the plasma membrane under ligand bound conditions. A bimolecular fluorescence complementation (BiFC) assay was established by fusing the N- and C-terminal fragments of Venus to the cytoplasmic tail of OX40, enabling fluorescence reconstitution upon receptor self-association (Fig. 3E). Because the assay requires paired constructs, BiFC was performed for WT and the double mutant 2R-S, the variant that exhibited the strongest functional defect. Upon stimulation with the naturally occurring trimeric OX40L ectodomain (OX40L), both WT and 2R-S showed robust Venus reconstitution, with comparable fluorescence intensity (Fig. 3F), indicating that R241/R242 are not required for ligand-induced receptor clustering. These results indicate that substitution of R241/R242 does not impair the ability of OX40 to cluster at the plasma membrane.

Having excluded reduced effects on receptor stability or clustering, we next evaluated signaling output. As a member of the TNFR superfamily, OX40 requires ligand-induced receptor multimerization to recruit TRAF adaptors and activate the canonical NF-κB pathway. To standardize receptor activation in cells, we stimulated HeLa NF-κB reporter lines expressing WT or mutant OX40 with TNC-scOX40L, a tenascin-C-fused single-chain OX40L agonist designed to promote multivalent receptor clustering (Appendix Fig. S3I–K). Similar tenascin-C-fused single-chain TNF ligand formats have previously been used to enhance TNFR family receptor activation, including in studies of TNFR2 signaling (Rauert et al, 2011; Rauert et al, 2010). The ligand formats, sources, and stimulation concentration ranges used for the reporter assays are summarized in Table 1. Flow cytometry analysis further showed comparable cell surface Flag-OX40 binding across WT and BRS mutant receptors (Fig. 3G; Appendix Fig. S3D–H), indicating that BRS mutation does not reduce receptor abundance at the plasma membrane. Dose response analyses revealed that the single mutations R241S and R242S markedly reduced ligand-induced NF-κB activation. In contrast, the double mutant 2R-S completely failed to activate NF-κB across all ligand concentrations tested (Fig. 3H,I). These results demonstrate that the conserved juxtamembrane arginine residues R241 and R242 are jointly required for productive OX40 signal transduction, despite preserved surface expression, intact ligand-induced clustering, and delayed rather than accelerated receptor degradation.

Membrane anchoring by the OX40 basic residue rich sequence promotes efficient canonical NF-κB and PI3K-AKT signaling

In the preceding section, we showed that mutations within the juxtamembrane basic residue rich sequence (BRS) of OX40 markedly attenuate downstream signaling. To define which signaling nodes are specifically affected, we systematically examined key molecular markers within OX40 mediated pathways. Upon ligand engagement, OX40 recruits TRAF2 to activate the IKK complex, leading to phosphorylation and degradation of IκBα,

 © The Author(s)


A
A236 L237 Y238 L239 L240 R241 D243 Q244 R245 L246 D249 A250 H251 G255 G257 S258 F259 R260 T261 I263 Q264 E265 E266 Q267 A268 D269 A270 H271 S272 T273 L274 A275 K276 I277
DMPG
1 2 3 4 5 6 7 8
^{1}H-ind(ppm)
^{1}H-acq(ppm)
B
FRET emission (593 nm)
Excitation (463 nm)
NH₂ NH₂ NH₂
Amine Labeling
Rhodamine
NBD-Liposome
C
Normalized FRET Intensity
0.6 0.5 0.4 0.3
****
****
****
WT Y-A 2R-S Y-A/2R-S Y-A/3R-S NBD CT
D
R1 (S^{-1})
R2 (S^{-1})
NOE
In Solution
In DMPG
2.0 1.5 1.0 0.5 0.0
25 20 15 10 5 0
1.0 0.5 0 -0.5 -1.0
236 246 256 266 276
Residue Number

© The Author(s)

Figure 2. Membrane insertion stabilizes the OX40 juxtamembrane domain through R241/R242 mediated interactions.

(**A**) Intermolecular nuclear Overhauser effects (NOEs) between $OX40_{236-277}$ backbone amides and DMPG acyl chains. Shown are strips from 3D ^{15}N edited NOESY TROSY-HSQC spectra (τNOE = 200 ms) of 0.8 mM [^{15}N, ^{2}H]-labeled $OX40_{236-277}$ in DMPG/d-DH6PC bicelles ($q = 0.8$), recorded at 800 MHz. NOEs exclusively arise from interactions between protein amide protons and protonated DMPG lipids. (**B**) Schematic of FRET assay probing $OX40_{236-277}$ DMPG interactions. $OX40_{236-277}$ was randomly labeled with NHS-Rhodamine (*acceptor*), and NBD-PE (*donor*) was incorporated into DMPG liposome at a 10:1 (DMPG: NBD-PE) molar ratio. (**C**) Normalized FRET efficiency comparison between WT $OX40_{236-277}$ and mutants (Y238A, R241S/R242S indicated as 2R-S, Y238A/R241S/R242S indicated as Y-A/2R-S, and Y238A/R241S/R242S/R245S indicated as Y-A/3R-S) binding to PG liposomes. NBD-PE containing liposomes without protein served as negative control. Data are presented as mean ± SD ($n = 3$ independent protein preparations). Statistical analysis was performed using one-way ANOVA followed by Dunnett's multiple comparisons test. Exact adjusted *P* values were: WT vs. 2R-S, $P = 8.13 \times 10^{-10}$; WT vs. Y-A/2R-S, $P = 1.47 \times 10^{-8}$; WT vs. Y-A/3R-S, $P = 9.16 \times 10^{-9}$. (**D**) Dynamics of membrane bound $OX40_{236-277}$. ^{15}N relaxation parameters (longitudinal *R*1, transverse *R*2, and ^{1}H-^{15}N heteronuclear NOEs) measured for $OX40_{236-277}$ in DMPG bicelles. Source data are available online for this figure.

subsequent NF-κB activation, and promotion of T-cell proliferation and survival. In addition to this canonical cascade, previous studies have reported that OX40 signaling can also modulate the PI3K-AKT phosphorylation cascade (So et al, 2011; Song et al, 2005; Zhang et al, 2021) (Appendix Fig. S4A). To validate the functional readouts observed in the NF-κB luciferase reporter assay, we therefore assessed the phosphorylation status of critical downstream effectors by immunoblotting.

We first analyzed Jurkat T cells stably expressing wild-type (WT) OX40. To determine an appropriate stimulation window, cells were stimulated with TNC-scOX40L for 0, 5, 10, 15, 30, 60 and 120 min, followed by immunoblotting for p-AKT, total AKT, p-IκBα, total IκBα, p-p65 and total p65. OX40-WT induced rapid phosphorylation of AKT, IκBα and p65, with the strongest or near-strongest activation observed at approximately 10 min after stimulation (Fig. 4A–D). Based on this kinetic profile, we selected the 10-min time point for direct comparison between WT and BRS mutant receptors. Under this condition, substitution of either R241 or R242 markedly reduced phosphorylation of AKT, IκBα and p65 compared with WT, and the double mutant R241S/R242S (2R-S) showed the strongest overall impairment (Fig. 4E–H). These results indicate that the OX40 BRS is required for efficient early activation of both the canonical NF-κB pathway and the PI3K-AKT cascade in a T-cell context.

To determine whether this effect was also observed in the HeLa reconstitution system used for the reporter assays, we performed the same kinetic and mutant comparison analyses in HeLa cells stably expressing OX40 (Appendix Fig. S4B,C). Similar to Jurkat cells, OX40-WT induced time dependent phosphorylation of AKT, IκBα and p65 after TNC-scOX40L stimulation, with robust activation detected around 10 min (Fig. 4I–L). Direct comparison at this time point showed that R241S, R242S and 2R-S all reduced phosphorylation of these downstream markers relative to WT (Fig. 4M–P). Thus, the signaling defects caused by BRS mutation are reproducible in both T-cell-derived and reconstituted cell systems.

Taken together, these data show that the juxtamembrane arginines R241 and R242 are required for efficient early activation of canonical NF-κB and PI3K-AKT signaling. Combined with the preserved receptor surface expression, delayed rather than accelerated receptor turnover, and intact ligand-induced clustering described above, these results support a model in which BRS mediated membrane anchoring regulates productive OX40 signal initiation downstream of receptor engagement.

Disruption of the juxtamembrane basic motif impairs membrane-proximal OX40-TRAF2 engagement

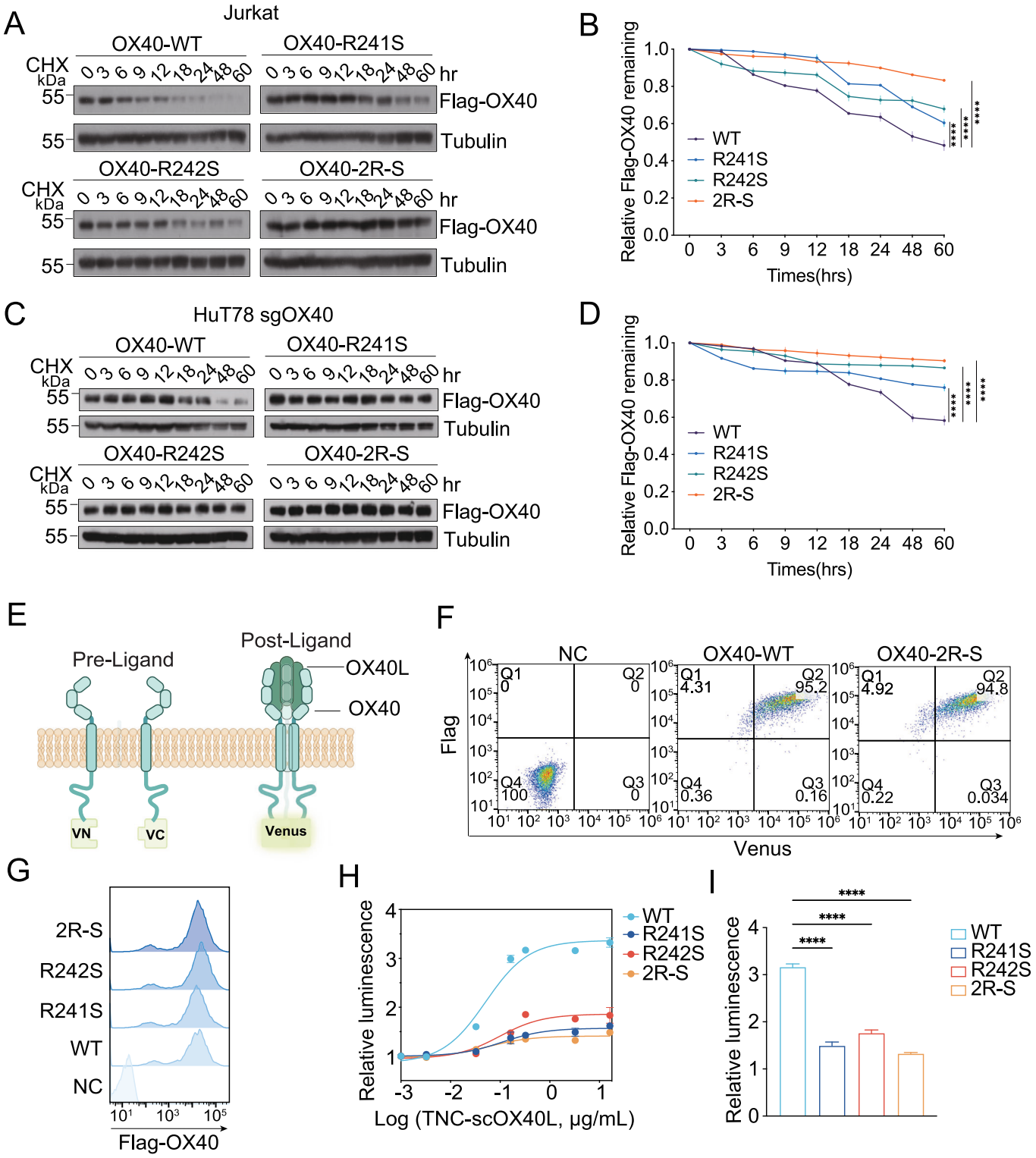
Given that substitution of R241 and R242 markedly attenuates OX40 signaling despite preserved receptor surface expression, intact ligand-induced clustering, and delayed rather than accelerated receptor turnover, we next asked whether the juxtamembrane basic residue rich sequence (BRS) impairs downstream signaling by disrupting TRAF2 engagement. To visualize receptor–adaptor organization at the plasma membrane, we generated stable HeLa cell lines co-expressing OX40-GFP and TRAF2-mCherry. Flow cytometry confirmed comparable OX40-GFP and TRAF2-mCherry expression across WT and BRS mutant cell lines (Appendix Fig. S5A).

Confocal imaging was then performed in the absence and presence of TNC-scOX40L stimulation. Under unstimulated conditions, OX40-WT showed clear membrane localization and detectable spatial overlap with TRAF2-mCherry at the cell periphery (Fig. 5A). Line-scan fluorescence intensity profiles across the membrane showed overlapping GFP and mCherry signals, consistent with basal membrane-proximal OX40-TRAF2 association (Fig. 5B). In contrast, the single mutants R241S and R242S retained OX40 membrane localization but showed reduced TRAF2 enrichment at OX40 positive membrane regions. The double mutant 2R-S showed the strongest reduction in OX40-TRAF2 spatial overlap. Quantification using Pearson's correlation coefficients confirmed reduced OX40-TRAF2 colocalization in BRS mutant cells under basal conditions (Appendix Fig. S5B).

We next examined whether ligand stimulation restores OX40-TRAF2 colocalization in the BRS mutants. Following TNC-scOX40L stimulation, WT OX40 maintained prominent membrane-proximal overlap with TRAF2-mCherry, whereas R241S, R242S, and 2R-S continued to show reduced TRAF2 colocalization at OX40-positive membrane regions (Fig. 5C,D). Pearson's correlation analysis further confirmed that BRS mutations reduced OX40-TRAF2 colocalization under ligand-stimulated conditions (Appendix Fig. S5C). These results indicate that mutation of R241/R242 impairs membrane-proximal OX40-TRAF2 organization both before and after ligand stimulation.

To determine whether the reduced colocalization reflects impaired receptor–adaptor complex formation, we performed co-immunoprecipitation assays using FLAG-tagged OX40 variants under both unstimulated and TNC-scOX40L stimulated conditions. In cells expressing OX40-WT, TRAF2 was readily detected, consistent with OX40-TRAF2 complex formation (Fig. 5E). In contrast, substitution of either R241 or R242 reduced the amount of TRAF2 recovered with OX40, and the 2R-S double mutant showed the strongest reduction. This defect was observed both in the absence and presence of TNC-scOX40L stimulation. Whole-cell extracts confirmed comparable total TRAF2 and Flag-OX40 expression across constructs, with tubulin serving as a loading control, indicating that the reduced co-immunoprecipitation signal

 © The Author(s)



reflects altered receptor–adaptor association rather than differences in protein abundance.

Notably, BRS mutation did not completely eliminate OX40-TRAF2 association, consistent with the presence of the canonical PIQEE TRAF2 binding motif in these constructs. Thus, the juxtamembrane BRS is best interpreted as a membrane-proximal regulatory element that promotes efficient and spatially constrained TRAF2 engagement, rather than as the sole TRAF2-binding determinant. Collectively, the imaging and co-immunoprecipitation data support a model in which R241/R242 mediated membrane anchoring facilitates productive OX40-TRAF2 complex assembly, providing a mechanistic explanation for the reduced NF-κB and PI3K-AKT signaling observed in BRS mutants.

© The Author(s)

Figure 3. Juxtamembrane arginines R241/R242 mediate OX40 dependent NF-κB activation without reducing receptor abundance or ligand-induced clustering.

(**A**, **B**) CHX chase assay in Jurkat stable cell lines expressing OX40 WT, R241S, R242S, or R241S/R242S (2 R-S). Cells were treated with cycloheximide (CHX, 100 μg/mL) for 0–60 h. (**A**) Immunoblots showing time-dependent degradation of OX40 proteins. (**B**) Quantification of relative OX40 levels normalized to tubulin, determined by densitometry (ImageJ). Data are mean ± SD from three independent biological replicates ($n = 3$ biological replicates). Statistical analysis was performed using two-way ANOVA followed by Dunnett's multiple comparisons test. Exact adjusted P values were: WT vs. R241S, $P = 2.1 \times 10^{-14}$; WT vs. R242S, $P = 2.1 \times 10^{-14}$; WT vs. 2R-S, $P = 2.1 \times 10^{-14}$. (**C**, **D**) CHX chase assay in HuT78 sgOX40 stable cell lines expressing the same OX40 variants, performed and analyzed as in Jurkat cell. (**C**) Immunoblots of time-dependent degradation. (**D**) Quantification of relative OX40 levels (normalized to tubulin). Data are mean ± SD from three independent biological replicates ($n = 3$ biological replicates). Statistical analysis was performed using two-way ANOVA followed by Dunnett's multiple comparisons test. Adjusted P values were: WT vs. R241S, $P = 2.47 \times 10^{-8}$; WT vs. R242S, $P < 1 \times 10^{-15}$; WT vs. 2R-S, $P < 1 \times 10^{-15}$. (**E**) Schematic of the Venus-based bimolecular fluorescence complementation (BiFC) assay. The N- (VN) and C-terminal (VC) fragments of Venus were fused to the OX40 cytoplasmic tail. (**F**) Representative flow cytometry plots of BiFC signals in HeLa cells expressing WT or 2R-S OX40, with OX40L stimulation. (**G**) Representative flow cytometry histograms showing cell surface Flag-OX40 binding across WT and mutant receptors in HeLa cells. (**H**, **I**) NF-κB luciferase reporter activity in HeLa cells expressing WT or mutant OX40 following stimulation with TNC-scOX40L. Dose-response curves in (**H**) and endpoint quantification at saturating TNC-scOX40L in (**I**) were derived from the same experiments. Data are mean ± SD ($n = 4$ independent biological experiments). Statistical comparison in (**I**) was performed by ordinary one-way ANOVA followed by Dunnett's multiple comparisons test. Adjusted P values were: WT vs. R241S, $P = 2.87 \times 10^{-13}$; WT vs. R242S, $P = 2.34 \times 10^{-12}$; WT vs. 2R-S, $P = 9.00 \times 10^{-14}$. Source data are available online for this figure.

Table 1. TNF Ligand formats, sources, and stimulation concentrations.

Ligand	Format	Source	Stimulation concentration range
OX40L	TNC-scOX40L	expressed and purified from Expi293F cells	0, 0.00325, 0.0325, 0.1625, 0.325, 3.25, 16.25 (μg/mL)
4-1BBL	4-1BBL	Purchased from ACRO Biosystems, His/Flag Tag, Cat# 41L-H52D4.	0, 0.00325, 0.0325, 0.1625, 0.325, 3.25, 16.25, 32.5 (μg/mL)
CD40L	CD40L	Purchased from ACRO Biosystems, Fc Tag, Cat# CDL-H5264.	0, 0.00325, 0.0325, 0.1625, 0.325, 3.25, 16.25 (μg/mL)

Membrane anchoring by the juxtamembrane basic motif creates a secondary TRAF2 contact site adjacent to the canonical PxQxx motif

OX40 activates the NF-κB signaling cascade through engagement of its conserved C-terminal motif "PIQEE" with TRAF2, a mechanism broadly conserved among TNFR superfamily costimulatory receptors (Matsuzawa et al, 2008; Ye and Wu, 2000). In OX40, however, this motif is spatially separated from the membrane-proximal basic residues R241 and R242 by a ~ 30 residue flexible loop. Our cellular analyses showed that disrupting these basic residues severely impairs TRAF2 recruitment and complex formation despite an intact PIQEE motif, suggesting that membrane anchoring by the BRS contributes to TRAF2 engagement beyond the canonical interface.

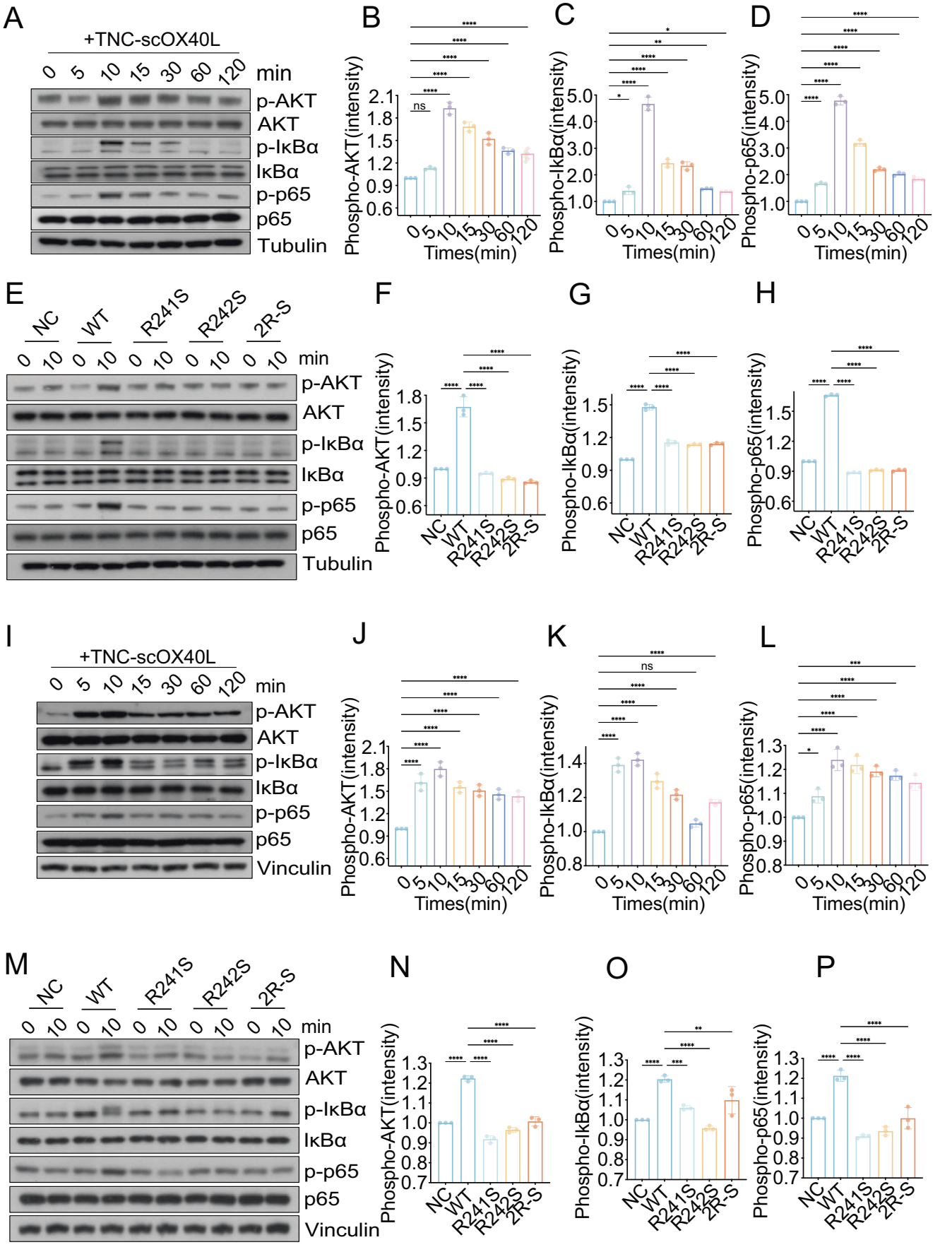
To dissect this mechanism at residue resolution, we recombinantly purified the TRAF2 C-terminal domain (TRAF2-C), known to specifically recognize the PIQEE motif, and established a membrane mimetic system in which the cytoplasmic tail of OX40 (OX40-CTD) was anchored to phosphatidylglycerol (PG) lipid nanodisc. Residue resolved HSQC peak intensity ratios of OX40-CTD in solution confirmed selective signal attenuation at the PIQEE motif upon TRAF2-C binding while the membrane-proximal region remained largely unaffected (Fig. 6A; Appendix Fig. S6A), consistent with previously reported structural data (McWhirter et al, 1999; Ye et al, 1999). Direct overlay of free OX40-CTD with PG-NDC associated OX40-CTD further confirmed chemical shift perturbations around the BRS region upon nanodisc association (Appendix Fig. S6B). In contrast, when OX40-CTD was lipid nanodisc anchored, TRAF2-C binding induced additional signal broadening in residues surrounding the BRS, indicating the presence of a secondary TRAF2 engaging region in the membrane-proximal region (Fig. 6B; Appendix Fig. S6C).

We further assessed this interaction by incrementally titrating TRAF2-C into the PG-nanodisc bound OX40-CTD. Peaks corresponding to both the canonical TRAF2 interface (E265) and the BRS-proximal region (Y238) exhibited concentration dependent broadening and intensity loss, whereas residues outside these sites (G257, I277) showed only minimal changes (Fig. 6C). These observations suggest that membrane bound OX40-CTD promotes TRAF2 membrane targeting through cooperative interactions at two spatially distinct regions (Fig. 6D). Consistent with this model, substitution of R241 and R242 abolished signal perturbations in the juxtamembrane region, confirming that basic-residue mediated membrane anchoring is essential for formation of the proximal TRAF2 interface (Appendix Fig. S6D–H).

To directly quantify this effect on binding affinity, we performed bio-layer interferometry using PG-nanodisc-reconstituted OX40-CTD. TRAF2 bound OX40 WT with a dissociation constant of $K_D = 1.27$ μM, whereas the double mutant OX40 2R-S (R241S/R242S) displayed a dramatically weakened affinity ($K_D = 117.1$ μM) (Fig. 6E,F). To further distinguish the contribution of the BRS from that of the canonical PIQEE motif, we analyzed an OX40-CTD mutant in which the PIQEE motif was disrupted. Mutation of the PIQEE motif reduced but did not abolish TRAF2 binding, with an apparent K_D of 39.98 μM, whereas the combined OX40-2R-S +3Mut construct showed little detectable TRAF2 binding (Appendix Fig. S6I,J). These data indicate that the membrane-proximal BRS provides a PIQEE independent contribution to TRAF2 engagement, while both the BRS and the canonical PIQEE motif are required for maximal OX40-TRAF2 binding.

The physiological relevance of this mechanism was assessed using fluorescence resonance energy transfer (FRET) measurements in cells. Full length TRAF2 fused to monomeric teal fluorescent protein (mTFP) was stably expressed in cells expressing OX40-WT, R241S, R242S, or the double mutant 2R-S, and plasma membranes were labeled with the lipophilic dye R18. FRET efficiencies measured by donor dequenching revealed a marked reduction in membrane-proximal TRAF2 localization in all three BRS mutants, with the double mutant exhibiting the strongest loss of FRET relative to WT (Fig. 6G,H). These results indicate that R241 and R242 are required to maintain TRAF2 proximity to the

 © The Author(s)


A
+TNC-scOX40L
0 5 10 15 30 60 120 min
p-AKT
AKT
p-IκBα
IκBα
p-p65
p65
Tubulin
B
Phospho-AKT(intensity)
Times(min)
C
Phospho-IkBα(intensity)
Times(min)
D
Phospho-p65(intensity)
Times(min)
E
NC WT R241S R242S 2R-S
0 10 0 10 0 10 0 10 0 10 min
p-AKT
AKT
p-IκBα
IκBα
p-p65
p65
Tubulin
F
Phospho-AKT(intensity)
NC WT R241S R242S 2R-S
G
Phospho-IkBα(intensity)
H
Phospho-p65(intensity)
I
+TNC-scOX40L
0 5 10 15 30 60 120 min
p-AKT
AKT
p-IκBα
IκBα
p-p65
p65
Vinculin
J
Phospho-AKT(intensity)
Times(min)
K
Phospho-IkBα(intensity)
Times(min)
L
Phospho-p65(intensity)
Times(min)
M
NC WT R241S R242S 2R-S
0 10 0 10 0 10 0 10 0 10 min
p-AKT
AKT
p-IκBα
IκBα
p-p65
p65
Vinculin
N
Phospho-AKT(intensity)
NC WT R241S R242S 2R-S
O
Phospho-IkBα(intensity)
P
Phospho-p65(intensity)

© The Author(s)

Figure 4. Immunoblotting reveals loss of NF-κB and PI3K-AKT activation upon disruption of OX40 membrane anchoring.

(**A**) Representative immunoblots of Jurkat cells expressing wild-type (WT) OX40 stimulated with multivalent TNC-scOX40L (3.25 μg/mL) for the indicated times (0, 5, 10, 15, 30, 60, 120 min). Total and phosphorylated AKT, IκBα, and p65 were detected; Tubulin served as loading control. Strong activation was observed at 10 min, which was therefore chosen as the optimal time point for subsequent mutant comparisons. (**B–D**) Quantification of phospho-AKT (**B**), phospho-IκBα (**C**), and phospho-p65 (**D**) band intensities from (**A**), normalized to total protein levels and to the 0 min control. Data are presented as mean ± SD from three independent biological experiments ($n = 3$). Statistical analysis was performed using ordinary one-way ANOVA followed by Dunnett's multiple comparisons test. Adjusted P values were: for phospho-AKT, 0 vs. 5 min, $P = 0.0655$; 0 vs. 10 min, $P = 5.76 \times 10^{-11}$; 0 vs. 15 min, $P = 3.46 \times 10^{-9}$; 0 vs. 30 min, $P = 1.17 \times 10^{-7}$; 0 vs. 60 min, $P = 9.41 \times 10^{-6}$; 0 vs. 120 min, $P = 3.36 \times 10^{-5}$. For phospho-IκBα, 0 vs. 5 min, $P = 0.0122$; 0 vs. 10 min, $P = 5.60 \times 10^{-14}$; 0 vs. 15 min, $P = 1.66 \times 10^{-8}$; 0 vs. 30 min, $P = 4.05 \times 10^{-8}$; 0 vs. 60 min, $P = 0.00324$; 0 vs. 120 min, $P = 0.0214$. For phospho-p65, 0 vs. 5 min, $P = 1.48 \times 10^{-6}$; 0 vs. 10 min, $P = 2.00 \times 10^{-15}$; 0 vs. 15 min, $P = 2.26 \times 10^{-13}$; 0 vs. 30 min, $P = 7.53 \times 10^{-10}$; 0 vs. 60 min, $P = 6.28 \times 10^{-9}$; 0 vs. 120 min, $P = 8.90 \times 10^{-8}$. (**E**) Representative immunoblots of Jurkat cells expressing WT OX40 or the BRS mutants (R241S, R242S, R241S/R242S [2R-S]) stimulated with TNC-scOX40L (3.25 μg/mL) for 0 or 10 min. Antibodies and loading control as in (**A**). (**F–H**) Quantification of phospho-AKT (**F**), phospho-IκBα (**G**), and phospho-p65 (**H**) band intensities from (**E**), normalized to total protein levels and WT control at 10 min. Data are presented as mean ± SD from three independent biological experiments ($n = 3$). Statistical analysis was performed using ordinary one-way ANOVA followed by Dunnett's multiple comparisons test. Adjusted P values were: for phospho-AKT, WT vs. NC, $P = 4.88 \times 10^{-8}$; WT vs. R241S, $P = 2.47 \times 10^{-8}$; WT vs. R242S, $P = 1.14 \times 10^{-8}$; WT vs. 2R-S, $P = 7.40 \times 10^{-9}$. For phospho-IκBα, WT vs. NC, $P = 1.69 \times 10^{-11}$; WT vs. R241S, $P = 8.10 \times 10^{-10}$; WT vs. R242S, $P = 4.46 \times 10^{-10}$; WT vs. 2R-S, $P = 5.59 \times 10^{-10}$. For phospho-p65, WT vs. NC, WT vs. R241S, WT vs. R242S, and WT vs. 2R-S, $P < 1 \times 10^{-15}$ for all comparisons. (**I**) Representative immunoblots of HeLa cells expressing WT OX40, stimulated and analyzed as in (**A**). Again, 10 min was identified as the optimal time point for subsequent experiments. (**J–L**) Quantification of phospho-AKT (**J**), phospho-IκBα (**K**), and phospho-p65 (**L**) band intensities from (**I**), normalized to total protein levels and to the 0 min control. Data are presented as mean ± SD from three independent biological experiments ($n = 3$). Statistical analysis was performed using ordinary one-way ANOVA followed by Dunnett's multiple comparisons test. Adjusted P values were: for phospho-AKT, 0 vs. 5 min, $P = 6.68 \times 10^{-7}$; 0 vs. 10 min, $P = 2.55 \times 10^{-8}$; 0 vs. 15 min, $P = 2.45 \times 10^{-6}$; 0 vs. 30 min, $P = 6.40 \times 10^{-6}$; 0 vs. 60 min, $P = 2.17 \times 10^{-5}$; 0 vs. 120 min, $P = 4.15 \times 10^{-5}$. For phospho-IκBα, 0 vs. 5 min, $P = 1.13 \times 10^{-9}$; 0 vs. 10 min, $P = 4.05 \times 10^{-10}$; 0 vs. 15 min, $P = 4.35 \times 10^{-8}$; 0 vs. 30 min, $P = 2.02 \times 10^{-6}$; 0 vs. 60 min, $P = 0.258$; 0 vs. 120 min, $P = 2.96 \times 10^{-5}$. For phospho-p65, 0 vs. 5 min, $P = 0.0118$; 0 vs. 10 min, $P = 4.94 \times 10^{-7}$; 0 vs. 15 min, $P = 1.51 \times 10^{-6}$; 0 vs. 30 min, $P = 7.67 \times 10^{-6}$; 0 vs. 60 min, $P = 2.17 \times 10^{-5}$; 0 vs. 120 min, $P = 0.000164$. (**M**) Representative immunoblots of HeLa cells expressing WT OX40 or the BRS mutants (R241S, R242S, 2 R-S), stimulated and analyzed as in (**E**). (**N–P**) Quantification of phospho-AKT (**N**), phospho-IκBα (**O**), and phospho-p65 (**P**) band intensities from (**M**), normalized to total protein levels and to the WT control at 10 min, as in (**F–H**). Data are presented as mean ± SD from three independent biological experiments ($n = 3$). Statistical analysis was performed using ordinary one-way ANOVA followed by Dunnett's multiple comparisons test. Adjusted P values were: for phospho-AKT, WT vs. NC, $P = 2.93 \times 10^{-8}$; WT vs. R241S, $P = 1.39 \times 10^{-9}$; WT vs. R242S, $P = 7.04 \times 10^{-9}$; WT vs. 2R-S, $P = 4.14 \times 10^{-8}$. For phospho-IκBα, WT vs. NC, $P = 5.45 \times 10^{-5}$; WT vs. R241S, $P = 0.000960$; WT vs. R242S, $P = 1.02 \times 10^{-5}$; WT vs. 2R-S, $P = 0.00829$. For phospho-p65, WT vs. NC, $P = 1.48 \times 10^{-5}$; WT vs. R241S, $P = 5.47 \times 10^{-7}$; WT vs. R242S, $P = 1.30 \times 10^{-6}$; WT vs. 2R-S, $P = 1.47 \times 10^{-5}$. Source data are available online for this figure.

plasma membrane, a prerequisite for efficient downstream NF-κB activation.

Together, these findings delineate a noncanonical mechanism in which the membrane-proximal BRS functions not only as a lipid anchoring module but also as a spatial organizer that positions TRAF2 in close proximity to its primary PIQEE binding site, thereby enhancing the apparent affinity and productive assembly of the receptor–adaptor complex. This secondary membrane dependent interface provides a PIQEE independent contribution but cooperates with, rather than replaces, the classical PxQxx motif, revealing an additional regulatory layer governing TNFR signal transduction.

Juxtamembrane basic residues support NF-κB activation across costimulatory TNFRs

Previous studies have shown that basic residues in the membrane-proximal regions of other TNFR superfamily members, such as 4-1BB and CD40, are also essential for TRAF2 membrane recruitment and downstream NF-κB signaling. These observations suggest that juxtamembrane basic residue rich sequences (BRS) may represent a broadly conserved regulatory module among costimulatory TNFRs (Fig. 7A). Besides OX40, additional costimulatory receptors, including 4-1BB, CD27, TNFR2, and CD40, also activate NF-κB signaling through TRAF engagement, typically via a conserved intracellular PxQxx motif. Owing to their potent immunostimulatory capacity, these cytoplasmic domains have been widely incorporated into CAR-T designs, contributing to the development of multiple CAR generations.

Building on our findings in OX40, we considered whether membrane-proximal BRS elements might similarly support NF-κB activation across other costimulatory TNFRs. A sequence alignment of representative family members revealed that these juxtamembrane regions are consistently enriched in basic residues, primarily arginine and lysine, positioned immediately adjacent to the transmembrane domain. To explore their functional significance, we established NF-κB luciferase reporter HeLa cell lines expressing mutant forms of 4-1BB and CD40 (Appendix Fig. S7). Upon stimulation with their respective ligands, WT 4-1BB and CD40 each exhibited robust, dose-dependent canonical NF-κB activation (Fig. 7B,C). Sigmoidal response curves were observed across a broad concentration range, and EC_{50} values were determined for each receptor, confirming that all constructs were functionally competent and responsive to ligand stimulation in this system. Flow cytometry confirmed comparable cell surface Flag binding among WT and BRS-mutant 4-1BB and CD40 constructs (Appendix Fig. S7), indicating that reduced reporter activation was not caused by reduced receptor surface expression.

We first examined 4-1BB, a costimulatory TNFR that, like OX40, contains conserved juxtamembrane arginine residues immediately downstream of the transmembrane domain. Mutation of either R215 or R217 markedly reduced ligand-induced NF-κB activation, and combined mutation of both residues nearly abolished the reporter response (Fig. 7D). We next tested whether a similar principle applies to CD40, whose juxtamembrane BRS is enriched in lysine rather than arginine residues. Mutation of four conserved lysines in this region strongly impaired CD40L-induced NF-κB activation (Fig. 7E). Together, these results indicate that membrane-proximal basic residues, whether arginine- or lysine-enriched, support efficient ligand-induced NF-κB activation across distinct costimulatory TNFRs. Although further receptor specific studies will be required to define the precise adaptor recruitment mechanism for each receptor, these data support a broader role for juxtamembrane basic motifs in TNFR signal regulation. This

 © The Author(s)

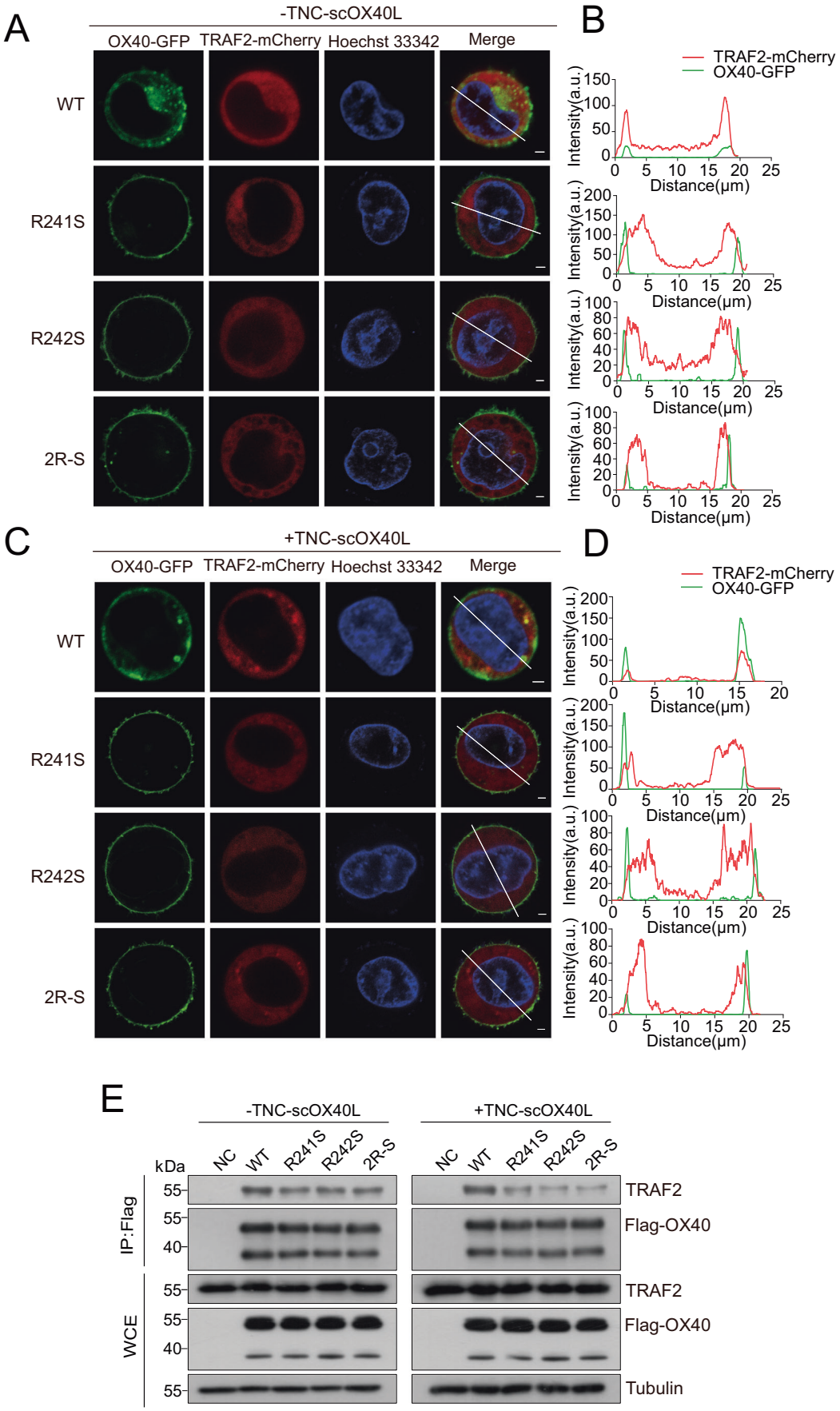

A
-TNC-scOX40L
OX40-GFP
TRAF2-mCherry
Hoechst 33342
Merge
WT
R241S
R242S
2R-S
B
TRAF2-mCherry
OX40-GFP
Intensity(a.u.)
Distance(μm)
C
+TNC-scOX40L
D
E
-TNC-scOX40L
+TNC-scOX40L
kDa
NC
WT
R241S
R242S
2R-S
IP:Flag
WCE
55
40
TRAF2
Flag-OX40
Tubulin

Figure 5. Juxtamembrane basic residues promote membrane-proximal OX40-TRAF2 engagement.

(**A**) Confocal fluorescence images of HeLa cells co-expressing OX40-GFP and TRAF2-mCherry under unstimulated conditions. OX40-GFP is shown in green, TRAF2-mCherry in red, and Hoechst 33342 nuclear staining in blue. White lines in the merged images indicate the regions used for line-scan analysis. Scale bars, 2 μm. Quantification is shown in Appendix Fig. S5B. (**B**) Line-scan fluorescence intensity profiles corresponding to the white lines in (**A**). (**C**) Confocal fluorescence images of HeLa cells co-expressing OX40-GFP and TRAF2-mCherry after stimulation with TNC-scOX40L (3.25 μg/mL, 16 h). Images are displayed as in (**A**). Quantification is shown in Appendix Fig. S5C. (**D**) Line-scan fluorescence intensity profiles corresponding to the white lines in (**C**). (**E**) Co-immunoprecipitation of endogenous TRAF2 with Flag-tagged OX40 variants. HeLa cells expressing Flag-tagged OX40-WT, R241S, R242S, or R241S/R242S (2R-S) were cultured with or without TNC-scOX40L stimulation (3.25 μg/mL, 16 h). Flag-OX40 was immunoprecipitated with anti-Flag antibody, and precipitated proteins were analyzed by immunoblotting for TRAF2 and Flag-OX40. Whole-cell extracts (WCE) were immunoblotted for TRAF2, Flag-OX40, and tubulin as a loading control. Source data are available online for this figure.

principle may operate alongside canonical TRAF binding motifs and should be considered when evaluating TNFR signaling or designing synthetic immunoreceptors.

Discussion

This study identifies a membrane anchoring mechanism within the juxtamembrane region of OX40 that is indispensable for downstream signaling. Integrated NMR spectroscopy, FRET analysis, and functional assays demonstrate that two evolutionarily conserved arginines, R241 and R242, drive specific interactions with anionic phospholipids and neighboring aliphatic residues, stabilizing the 236–242 segment in a membrane-inserted conformation. This lipid engagement imposes conformational rigidity on the cytoplasmic tail without reducing receptor surface expression or impairing ligand-induced oligomerization. Disrupting this anchoring mechanism by point mutations markedly attenuates NF-κB and PI3K-AKT activation in HeLa and Jurkat cell contexts, establishing membrane-proximal basic residues as essential determinants of productive OX40 signaling.

A key mechanistic insight emerging from this work is that the juxtamembrane basic residue rich sequence (BRS) forms an auxiliary, membrane dependent TRAF2 contact surface that operates in cooperation with the canonical C-terminal PxQxx motif. Residue resolved perturbation mapping of membrane-reconstituted OX40-CTD shows selective broadening within 236–242 upon TRAF2-C binding, consistent with the emergence of a secondary interaction region that is absent in solution. BLI measurements further indicate that disruption of R241 and R242 reduces TRAF2 affinity by approximately two orders of magnitude, and live cell FRET reveals impaired membrane-proximal TRAF2 localization in BRS mutants. Together, these data support a cooperative dual-site model in which membrane anchoring not only stabilizes receptor topology but also helps position the distal PIQEE motif for efficient engagement with the canonical TRAF2-C binding groove, thereby enhancing binding avidity and spatial organization at the membrane interface (Fig. 8). In this model, the BRS first engages negatively charged phospholipids at the inner leaflet and creates a membrane-proximal environment that favors TRAF2-C engagement, while the PIQEE motif remains the primary canonical TRAF2-binding element. Notably, BRS mutations only modestly reduce bulk TRAF2 association detected by co-immunoprecipitation, consistent with retention of the canonical PIQEE motif. However, proximity-sensitive assays reveal impaired membrane-proximal engagement, indicating that the BRS enhances spatially constrained adaptor assembly rather than serving as the primary binding interface. This distinction reconciles the limited change in co-IP with the more pronounced reduction in downstream signaling.

The broader significance of this membrane dependent regulatory module is reinforced by its conservation across multiple TNFR family costimulatory receptors. Systematic mutagenesis in 4-1BB and CD40 reveals that mutation of juxtamembrane basic residues diminishes NF-κB activation, phenocopying the OX40 BRS mutant phenotype and supporting a role for these motifs in efficient ligand-induced NF-κB activation. Notably, these basic clusters include both arginine- and lysine-rich motifs, suggesting that enrichment of positively charged residues is a common feature associated with membrane anchoring and adaptor positioning, although the detailed contribution of individual side chains remains to be determined. Together, these features support a conserved dual-site regulatory model within the TNFR superfamily, operating alongside the canonical PxQxx motif to fine-tune signaling strength.

Our findings refine current models of TNFR signal integration by establishing the BRS as a cooperative, membrane anchored signaling element. This conceptual advance underscore the importance of membrane composition and lipid engagement in shaping receptor architecture and adaptor recruitment. Beyond mechanistic insight, these results have direct translational implications. Current CAR-T constructs incorporating TNFR-derived intracellular domains predominantly emphasize the PxQxx motif as the principal driver of signal transduction. The present study suggests that failure to recapitulate native membrane anchoring features may limit TRAF docking efficiency and downstream signaling output. Rational incorporation of conserved BRS elements into synthetic receptors could enhance activation thresholds, modify tonic signaling, improve T cell persistence, and increase cytotoxicity in adoptive cell therapy. Furthermore, the membrane dependent dual-site mechanism may provide a generalizable framework for tuning receptor sensitivity or creating microenvironment selective signaling responses, especially in tissues with heterogeneous anionic lipid distribution.

While these data define the BRS as a membrane anchored module that couple lipid engagement to TRAF2 recruitment, the atomic determinants of OX40-TRAF2 recognition remain unresolved. In particular, the present data do not determine whether TRAF2-C uses two fully separate binding surfaces to recognize the BRS and PIQEE motifs, or whether membrane anchoring promotes a composite or dynamic interface. Future structural studies, such as cryo-EM analysis of the OX40L-OX40-TRAF2 complex, together with crosslinking mass spectrometry or molecular dynamics simulations, will be essential to delineate the geometry of this dual-site arrangement and to reveal how receptor clustering and lipid heterogeneity influence higher order signaling assemblies. Such efforts will further clarify how membrane-anchoring modules

 © The Author(s)

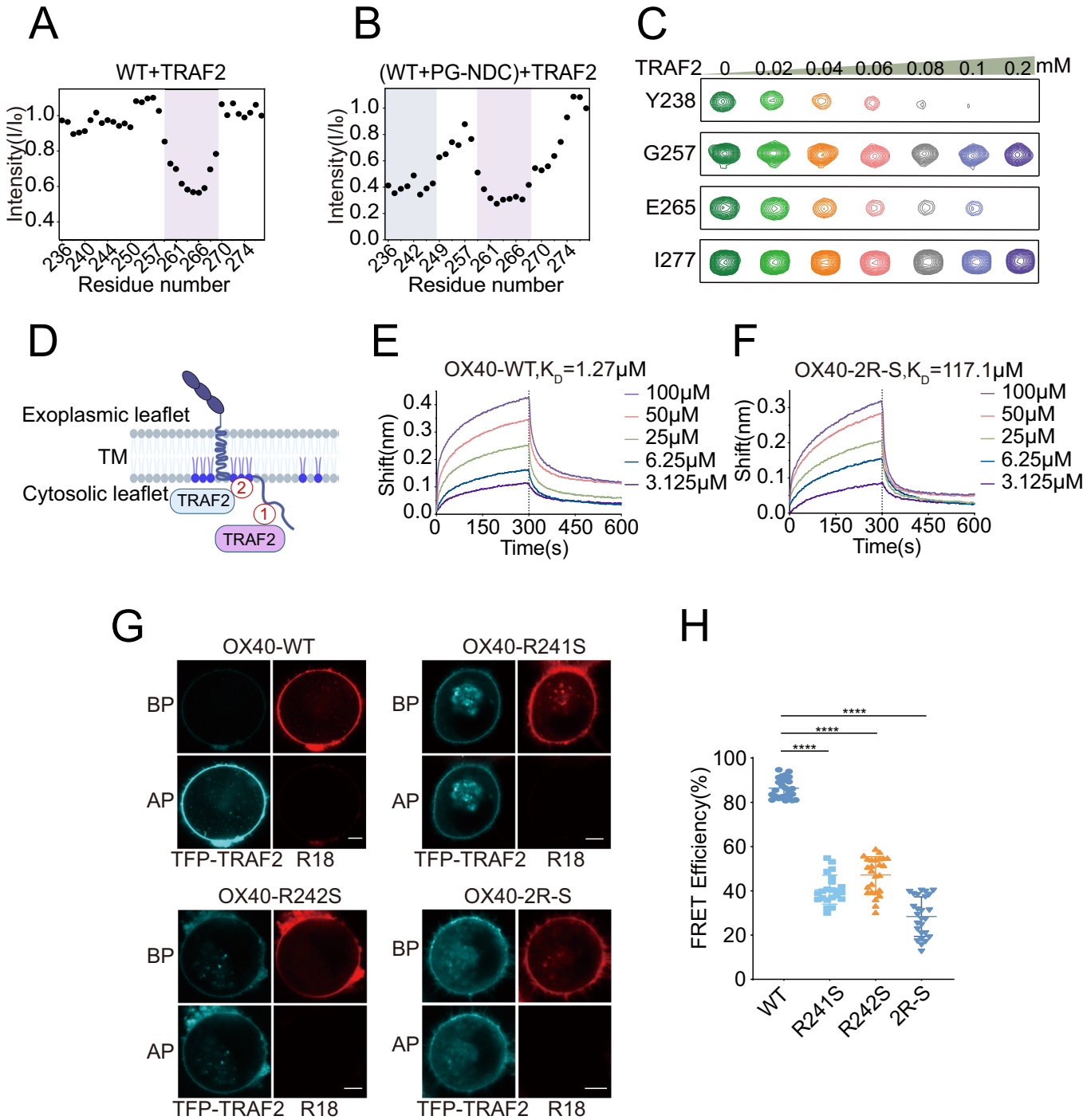


Figure 6. Membrane anchored R241/R242 residues potentiate TRAF2 recruitment in cooperation with the canonical PxQxx motif.

(**A**, **B**) Residue-resolved ^{1}H-^{15}N HSQC peak intensity ratios (I/I_0) of ^{15}N-labeled OX40 cytosolic tail (residues 236–277) upon titration with TRAF2 in the absence (**A**) or presence (**B**) of phosphatidylglycerol nanodiscs (PG-NDC). The shaded gray region marks the membrane-proximal BRS (residues 236–242); the purple region highlights the distal TRAF2 contact site (260–272). PG-NDC enhances signal attenuation across the TRAF2 interface. (**C**) Representative HSQC peaks (Y238, G257, E265, I277) showing progressive broadening and intensity loss during TRAF2 titration (0-0.2 mM), with Y238 and E265 displaying strong interface specific perturbation. (**D**) Schematic model: the BRS anchors the OX40 tail to the cytosolic leaflet (2), which in turn supports cooperative engagement with the distal TRAF2-binding interface (1). (**E**, **F**) Bio-layer interferometry sensorgrams of TRAF2 binding to OX40 reconstituted in PG-NDC nanodiscs. Curves show the association and dissociation of TRAF2 with OX40 WT (**E**; $K_D = 1.27$ μM) and with the double BRS mutant OX40 2R-S (R241S/R242S) (**F**; $K_D = 117.1$ μM). (**G**) Live cell imaging of mTFP-tagged TRAF2 (cyan) and membrane dye R18 (red) in cells expressing OX40 wild-type (WT), R241S, R242S, or 2R-S. Scale bars, 5 μm. BP before photobleaching, AP after photobleaching. (**H**) Quantification of OX40-TRAF2 interaction by acceptor-photobleaching FRET. Each point represents the FRET efficiency measured from one individual cell. Data were pooled from three independent biological experiments. The total numbers of cells analyzed were $n = 26$ for WT, $n = 22$ for R241S, $n = 26$ for R242S, and $n = 26$ for 2R-S. Data are shown as mean ± SD. Statistical significance was determined by ordinary one-way ANOVA followed by Dunnett's multiple comparisons test. Adjusted P values were: WT vs. R241S, $P < 1 \times 10^{-15}$; WT vs. R242S, $P < 1 \times 10^{-15}$; WT vs. 2R-S, $P < 1 \times 10^{-15}$. Source data are available online for this figure.

© The Author(s)

integrate with canonical motifs to shape adaptor organization and diversify signaling outcomes across TNFR family receptors.

Methods

Reagents and tools table

Reagent/resource	Reference or source	Identifier or catalog number
Experimental models		
BL21(DE3)	Weidi	Cat# EC1002
DH5α	Weidi	Cat# DL1001
HEK 293 T	ATCC	Cat# CRL-3216
HeLa	ATCC	Cat# CCL-2
Jurkat	ATCC	Cat# TIB-152
Expi293F	Gibco	Cat# A14527
HuT78	ATCC	Cat# TIB-161
Recombinant DNA		
pET28a-Sumo-3C-OX40_CTD(WT)	This study	P43489
pET28a-Sumo-3C-OX40_CTD(Y-A)	This study	P43489
pET28a-Sumo-3C-OX40_CTD(2R-S)	This study	P43489
pET28a-Sumo-3C-OX40_CTD(Y-A/2R-S)	This study	P43489
pET28a-Sumo-3C-OX40_CTD (Y-A/3R-S)	This study	P43489
pET28a-Sumo-3C-OX40_CTD(3Mut)	This study	P43489
pET28a-Sumo-3C-OX40_CTD (2R-S/3Mut)	This study	P43489
pcDNA3.1-TNC-scOX40L	This study	P23510
pET28a-His-SUMO-3C-TRAF2 (310–501)	This study	Q12933
PLEX-Flag-OX40_WT	This study	P43489
PLEX-Flag-OX40_R241S	This study	P43489
PLEX-Flag-OX40_R242S	This study	P43489
PLEX-Flag-OX40_2R-S	This study	P43489
BiFC-PHAGE-OX40_WT-VC	This study	P43489
BiFC-PHAGE-OX40_WT-VN	This study	P43489
BiFC-PHAGE-OX40_2R-S-VC	This study	P43489
BiFC-PHAGE-OX40_2R-S-VN	This study	P43489
PLEX-OX40_WT-GFP	This study	P43489
PLEX-OX40_R241S-GFP	This study	P43489
PLEX-OX40_R242S-GFP	This study	P43489
PLEX-OX40_2R-S-GFP	This study	P43489
PLEX-TRAF2-mCherry	This study	Q12933
PLEX-mTFP-TRAF2	This study	Q12933
PLEX-Flag-4-1BB_WT	This study	Q07011
PLEX-Flag-4-1BB_R215S	This study	Q07011
PLEX-Flag-4-1BB_R217S	This study	Q07011
PLEX-Flag-4-1BB_2R-S	This study	Q07011
PLEX-Flag-CD40_WT	This study	P25942
PLEX-Flag-CD40_4K-S	This study	P25942
Antibodies		
Flag	HUABIO	Cat# M1403-2
AKT	Cell Signaling Technology	Cat# 9272
Phospho-AKT	Cell Signaling Technology	Cat# 4060
IκBα	Cell Signaling Technology	Cat# 4812
Phospho-IκBα	Cell Signaling Technology	Cat# 2859
P65	Cell Signaling Technology	Cat# 8242
Phospho-P65	Cell Signaling Technology	Cat# 3033
PI3K	Cell Signaling Technology	Cat# 4257 T
Phospho-PI3K	Cell Signaling Technology	Cat# 17366 T
TRAF2	Cell Signaling Technology	Cat# 4724 T
Vinculin	Millipore	Cat# V4505
Tubulin	Sigma-Aldrich	Cat# T5168
APC anti-DYKDDDDK Tag antibody	BioLegend	Cat# 637308
HRP-conjugated Goat anti-Mouse IgG(H + L)	Abclonal	Cat# AS003

© The Author(s)

Reagent/resource	Reference or source	Identifier or catalog number
HRP-conjugated Goat anti-Rabbit IgG(H + L)	Abclonal	Cat# AS014
Oligonucleotides and other sequence-based reagents		
sgRNA targeting human OX40	This study	5′-GCCGGGCTTCT ACAACGACG-3′
Chemicals, enzymes and other reagents		
Isopropyl Alcohol	Macklin	Cat# I811925
Kanamycin monosulfate	Sangon Biotech	Cat# A600286
Ampicillin, Sodium Salt	Sangon Biotech	Cat# A610028
Methanol	Macklin	Cat# M813895
isopropyl β-D-thiogalactopyranoside (IPTG)	Sangon Biotech	Cat# A600168
Ammonium chloride (^{15}N, 99%)	Cambridge Isotope Laboratories	Cat# NLM-467-5
D-Glucose (U-$^{13}C_6$, 99%)	Cambridge Isotope Laboratories	Cat# CLM-1396-10
Imidazole	Sangon Biotech	Cat# I5513
Phenylmethane sulfonylfluoride(PMSF)	Sangon Biotech	Cat# A610425
DMPG Lipid	Avanti Polar Lipids	Cat# 840445
DMPC Lipid	Avanti Polar Lipids	Cat# 850345
DH6PC Detergent	Avanti Polar Lipids	Cat# 850305
16-DSA	Sigma-Aldrich	Cat# 253596
Dithiothreitol(DTT)	Sangon Biotech	Cat# A620058
Penicillin-Streptomycin(100×)	Epizyme Biotech	Cat# CB010
Polybrene	Sigma-Aldrich	Cat# H9268
Cycloheximide(CHX)	AbMole	Cat# M4879
Octadecyl rhodamine B chloride (R18)	Invitrogen	Cat# O246
4-1BB Ligand	ACRO Biosystems	Cat# 41L-H52D4
CD40 Ligand	ACRO Biosystems	Cat# CDL-H5264
NBD-PE	Invitrogen	Cat# N360
DMSO	Sangon Biotech	Cat# A600163
Software		
Sparky	Goddard, UCSF	www.cgl.ucsf.edu/home/sparky
NMRPipe	Delaglio et al, 1995	www.ibbr.umd.edu/nmrpipe
CcpNmr	Vranken et al, 2005	http://www.ccpn.ac.uk
Origin	OriginLab	www.originlab.com
PyMOL	Schrodinger, LLC	www.pymol.org
Adobe Illustrator 2020	Adobe	www.adobe.com/products/illustrator
GraphPad Prism 6.01	GraphPad	www.graphpad.com/scientific-software/prism
FlowJo	Becton, Dickinson & Company	www.flowjo.com
SnapGene	GSL Biotech	www.snapgene.com
ImageJ 1.8.0	Wayne Rasband	www.imagej.nih.gov/ij
Other		
Hoechst 33342	Beyotime	Cat# C1029
4% Paraformaldehyde Fix Solution	Ruian Biotech	Cat# R04-07A
HisPur™ Ni-NTA	Thermo Fisher Scientific	Cat# 88223
DpnI	NEB	Cat# R0176S
KOD One™ PCR Master Mix	TOYOBO	Cat# KMM101
SnakeSkin™(3.5 K MWCO)	Thermo Fisher Scientific	Cat# 88244
SnakeSkin™(10 K MWCO)	Thermo Fisher Scientific	Cat# 88243
Slide-A-Lyzer™(3.5 K MWCO)	Thermo Fisher Scientific	Cat# 66330
Superdex 75 Increase 10/300 GL Column	Cytiva	Cat# 29148721
Superdex 200 Increase 10/300 GL Column	Cytiva	Cat# 28990944
Amicon Ultra Centrifugal Filter Units (30 K MWCO)	Millipore	Cat# UFC9030
Amicon Ultra Centrifugal Filter Units (10 K MWCO)	Millipore	Cat# UFC9010
Amicon Ultra Centrifugal Filter Units (3 K MWCO)	Millipore	Cat# UFC9003
Amicon Ultra Centrifugal Filter Units (3 K MWCO)	Millipore	Cat# UFC8003
HiPure Plasmid EF Mini Kit	Magen Biotech	Cat# P1112
HiPure Plasmid Maxi Kit	Magen Biotech	Cat# P1004
2X MultiF Seamless Assembly Mix	Abclonal	Cat# RK21020
Anti-Flag Nanobody Magarose Beads	Thermo Fisher Scientific	Cat # A36798
Polyethylenimine HCL Max, MW 40000	Polysciences	Cat # 24765
Dual-Luciferase Assay System	Promega	Cat #E1910
Protease inhibitor cocktail	AbMole	Cat # M5293
Bovine serum albumin, fraction V heat shock isolation	Millipore	Cat# A9647
Nonidet P-40	Sigma-Aldrich	CAS # 127087-87-0
Immobilon®-NC Transfer Membrane	Millipore	Cat# HATF00010

© The Author(s)

Reagent/resource	Reference or source	Identifier or catalog number
PageRuler Prestained Protein Ladder	Thermo Fisher Scientific	Cat# 26616
Deoxycholic acid, sodium salt	Sangon Biotech	Cat# A600150
Antifade Mounting Medium	Beyotime	Cat#P0126
Immobilon® ECL UltraPlus Western HRP Substrate	Millipore	Cat# WBULP-100ML

Recombinant protein expression and purification

OX40 cytoplasmic tail constructs

The pET28a-His-SUMO-3C-OX40-CTD plasmid was transformed into Escherichia coli BL21 (DE3) competent cells. A single colony was inoculated into 3 mL of LB medium and cultured at 37 °C with shaking at 220 rpm for 10–12 h. The preculture was harvested by centrifugation at 5000 rpm for 1 min, and the pellet was resuspended in M9 medium before being transferred into 50 mL M9 for overnight growth at 37 °C, 220 rpm. The following day, the culture was inoculated into 1 L M9 minimal medium and incubated at 37 °C until reaching an OD_{600} of 0.8–0.9. Protein expression was induced with 0.5 mM isopropyl β-D-thiogalactopyranoside (IPTG), followed by incubation at 25 °C and 220 rpm for 16 h. Cells were harvested by centrifugation at 5000 rpm for 10 min.

The cell pellet was resuspended in Lysis Buffer (20 mM Tris-HCl, pH 8.0, 150 mM NaCl) supplemented with 0.5 mM PMSF, using 40 mL buffer per liter of culture. Cells were disrupted by ultrasonication for 30 min on ice. The lysate was clarified by centrifugation, and the supernatant was supplemented with 10 mM imidazole before incubation with 2 mL pre-equilibrated Ni-NTA resin (equilibrated in Wash Buffer 1: Lysis Buffer with 10 mM imidazole) for 1 h at 4 °C with gentle rotation. The mixture was loaded onto a gravity column, and the resin was washed extensively with Wash Buffer 1 and subsequently with Wash Buffer 2 (Lysis Buffer with 20 mM imidazole) until no contaminant proteins were observed in the flow-through. The target protein was eluted using Elution Buffer (Lysis Buffer with 300 mM imidazole) until the eluate no longer contained protein.

For tag removal, 3 C protease was added at 1% (w/w, protease: protein), and the eluted sample was dialyzed against Lysis Buffer using a 3.5 kDa molecular weight cutoff membrane at 4 °C for 24 h with three buffer exchanges. After cleavage, the mixture was clarified by centrifugation at 12,000 rpm for 30 min at 4 °C. The supernatant was supplemented with 10 mM imidazole and reloaded onto a Ni-NTA column. The flow-through was collected, followed by washes with Wash Buffer 1 to ensure complete removal of nonspecific proteins. The combined flow-through and wash fractions containing the cleaved OX40-CTD were concentrated to 1–2 mL using a centrifugal concentrator and further purified by size-exclusion chromatography on a Superdex 75 Increase 10/300 GL column (Cytiva) equilibrated in FPLC Buffer (25 mM phosphate buffer, pH 6.5, 100 mM NaCl).

All plasmid constructs used for recombinant protein expression, lentiviral transduction, BiFC assays, imaging, and reporter assays are listed in Appendix Table S1.

TRAF2 C-terminal domain

The pET28a-His-SUMO-3C-TRAF2 plasmid was transformed into *Escherichia coli* BL21 (DE3) competent cells. A single colony was inoculated into 10 mL LB medium and cultured overnight at 37 °C with shaking at 220 rpm. The preculture was transferred into 1 L LB medium and grown at 37 °C until the optical density at 600 nm (OD_{600}) reached 0.8–0.9. Protein expression was induced with 0.5 mM isopropyl β-D-thiogalactopyranoside (IPTG), and cells were further incubated at 25 °C with shaking at 220 rpm for 16 h. Cells were harvested by centrifugation at 5000 rpm for 10 min at 4 °C.

The cell pellet was resuspended in Lysis Buffer (25 mM Tris-HCl, pH 6.5, 150 mM NaCl, 5 mM β-mercaptoethanol) freshly supplemented with 0.5 mM PMSF and protease inhibitor cocktail (1:100 dilution), using 40 mL buffer per liter of culture. Cells were lysed by ultrasonication on ice for 30 min. The clarified supernatant was incubated with 2 mL of pre-equilibrated Ni-NTA resin (equilibrated in Lysis Buffer) for 1 h at 4 °C with gentle rotation. The resin was transferred to a gravity flow column, washed thoroughly with Wash Buffer (Lysis Buffer containing 10 mM imidazole), and eluted with Elution Buffer (Lysis Buffer containing 300 mM imidazole) until no additional protein was detected in the eluate.

The eluted fractions were pooled and dialyzed overnight at 4 °C against Lysis Buffer using a 14 kDa molecular weight cutoff dialysis membrane. 3 C protease was added at 1% (w/w, enzyme: protein) prior to dialysis for tag cleavage. The digested sample was clarified by centrifugation at 12,000 rpm for 30 min at 4 °C, and the supernatant was incubated with 2 mL of Ni-NTA resin pre-equilibrated in Lysis Buffer for 1 h at 4 °C to remove the cleaved His-SUMO tag, uncleaved fusion protein, and protease. The mixture was passed through a gravity column three times. The flow-through and subsequent washes with Wash Buffer were collected and pooled.

The purified TRAF2 protein was concentrated to 4–5 mL using a centrifugal filter and further purified by size-exclusion chromatography on a Superdex 200 Increase 10/300 GL column (Cytiva) equilibrated in FPLC Buffer (25 mM phosphate buffer, pH 6.5, 100 mM NaCl). Protein purity was assessed by SDS-PAGE.

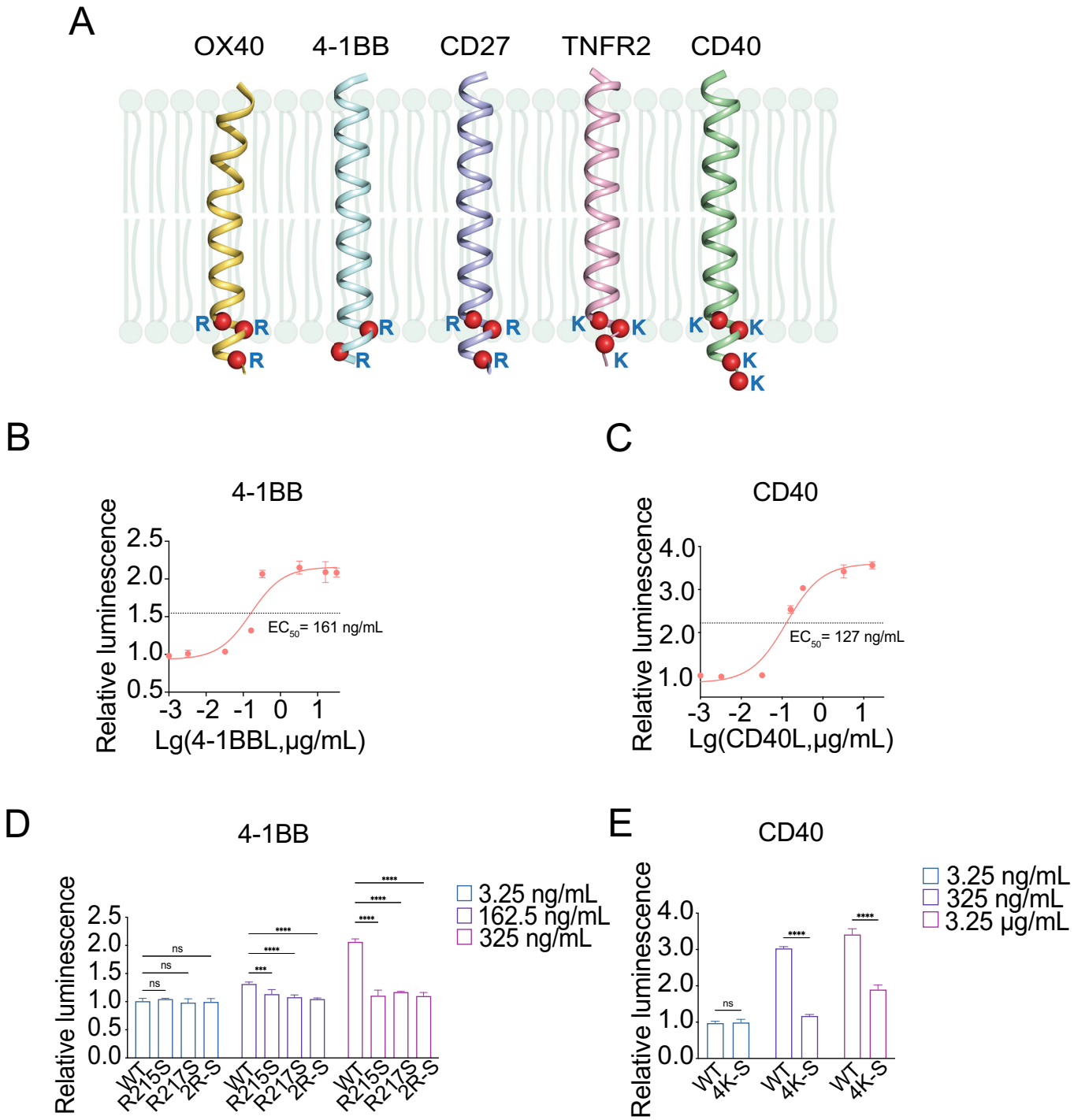
TRAF2 (310–501):

DQDKIEALSSKVQQLERSIGLKDLAMADLEQKVLEMEASTY DGVFIWKISDFARKRQEAVAGRIPAIFSPAFYTSRYGYKMCLRI YLNGDGTGRGTHLSLFFVVMKGPNDALLRWPFNQKVTLMLL DQNNREHVIDAFRPDVTSSSFQRPVNDMNIASGCPLFCPVSK-MEAKNSYVRDDAIFIKAIVDLTGL.

Assembly of bicelle based membrane mimetic systems

Long chain lipids 1,2-dimyristoyl-sn-glycero-3-phosphocholine (DMPC; Avanti, #850345) and 1,2-dimyristoyl-sn-glycero-3-phosphoglycerol (DMPG; Avanti, #840445) were each mixed with the short chain lipid 1,2-dihexanoyl-sn-glycero-3-phosphocholine (DH6PC; 6:0 PC; Avanti, #850305) at a 1:1.25 molar ratio after dissolution in chloroform. The mixtures were dried under a nitrogen stream to form thin films and lyophilized overnight. Lipid films were rehydrated in phosphate buffer (25 mM sodium phosphate, 100 mM NaCl, pH 6.5) to generate bicelles. OX40-CTD was incorporated at a 2:1 protein to bicelle molar ratio and incubated overnight. The bicelle size parameter q = [long chain lipid]/[DH_6PC] was adjusted, when necessary, by adding DH6PC

 © The Author(s)



or lowering its concentration through dialysis. NMR confirmed $q \approx 0.8$, which yields bilayer like topology with a planar region radius of ~34 Å.

Backbone resonance assignment using solution NMR

All NMR measurements were carried out at 30 °C using Agilent spectrometers operating at proton resonance frequencies of either 800 MHz or 600 MHz, both outfitted with cryogenically cooled probes. Spectral data were processed using the NMRPipe (Delaglio et al, 1995), and subsequent analysis was performed using XEASY (Bartels et al, 1995) and CcpNmr Analysis version 2 (Vranken et al, 2005). For sequence specific backbone resonance assignments of the OX40-CTD with and without bicelle, a series of TROSY enhanced triple resonance experiments were employed. These included HNCA, HN(CO)CA, HN(CA)CO, HNCO, HNCACB, and HN(CO)CACB (Kay et al, 2011;

© The Author(s)

Figure 7. Juxtamembrane basic residues support NF-κB activation across costimulatory TNFRs.

(**A**) Structural conservation of basic residue sequences (BRS). AlphaFold2 predicted membrane domains of representative TNFRs (OX40, 4-1BB, CD27, CD40, TNFR2) highlighting conserved arginine/lysine residues at the cytoplasmic juxtamembrane interface. (**B**, **C**) Dose response analysis of canonical NF-κB activation in HeLa cells stably expressing 4-1BB (**B**) and CD40 (**C**) upon stimulation with their respective ligands ($n = 4$ independent biological experiments for 4-1BB; $n = 6$ independent biological experiments for CD40). EC_{50} values are indicated for each receptor. (**D**) 4-1BB requires R215/R217 for signal competence. Analogous NF-κB reporter assays were performed using 4-1BB variants, including R215S, R217S, and the R215S/R217S double mutant (2R-S). Data are presented as mean ± SD from four independent biological experiments ($n = 4$). Statistical analysis was performed using ordinary one-way ANOVA followed by Dunnett's multiple comparisons test, performed separately at each ligand concentration. Adjusted P values were: at 3.25 ng/mL, WT vs. R215S, $P = 0.602$; WT vs. R217S, $P = 0.804$; WT vs. 2R-S, $P = 0.970$. At 162.5 ng/mL, WT vs. R215S, $P = 0.000427$; WT vs. R217S, $P = 3.92 \times 10^{-5}$; WT vs. 2R-S, $P = 1.06 \times 10^{-5}$. At 325 ng/mL, WT vs. R215S, $P = 1.58 \times 10^{-10}$; WT vs. R217S, $P = 3.61 \times 10^{-10}$; WT vs. 2R-S, $P = 1.47 \times 10^{-10}$. (**E**) Mutation of the lysine-based BRS in CD40 impairs NF-κB activation. The CD40 4K-S mutant (K216S/K217S/K220S/K221S) phenocopied the arginine mutants in OX40. Data are presented as mean ± SD. Statistical analysis was performed using independent samples t test at each ligand concentration. Exact P values were: at 3.25 ng/mL, WT vs. 4K-S, $P = 0.648$; at 325 ng/mL, WT vs. 4K-S, $P = 1.32 \times 10^{-12}$; at 3.25 µg/mL, WT vs. 4K-S, $P = 3.48 \times 10^{-9}$. The numbers of independent biological experiments were $n = 6$ for WT and $n = 5$ for 4K-S at 3.25 ng/mL, $n = 4$ for WT and $n = 6$ for 4K-S at 325 ng/mL, and $n = 6$ per group at 3.25 µg/mL. Source data are available online for this figure.

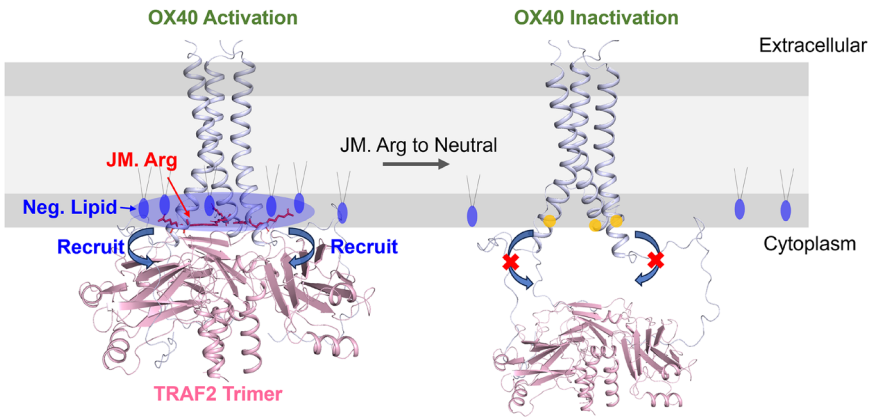


Figure 8. A lipid anchoring mechanism governs OX40 activation via juxtamembrane arginine residues.

A schematic model illustrating the role of juxtamembrane (JM) arginine residues in OX40 activation. (1) In the active state, positively charged JM arginine residues (red) engage with negatively charged phospholipids (blue ovals) at the inner leaflet of the plasma membrane, promoting a membrane conformation of the OX40 cytoplasmic tail. This lipid anchoring facilitates the recruitment of TRAF2 trimers (pink), enabling downstream signal transduction. (2) Upon mutating JM arginines to neutral residues, membrane interaction is weakened, leading to a disordered cytoplasmic tail and impaired TRAF2 engagement, thereby impairing OX40 signaling.

Salzmann et al, 1999). All spectra were recorded on a uniformly labeled (^{15}N, ^{13}C, 85% ^{2}H) OX40-CTD sample at 30 °C and a proton Larmor frequency of 600 MHz.

NMR chemical shift perturbation experiments

Mutant variants of OX40-CTD were prepared under identical conditions, and two-dimensional TROSY-HSQC spectra were recorded on an Agilent 800 MHz spectrometer. Residue specific combined chemical shift differences ($\Delta\delta^i_{comb}$) were calculated according to the equation (Schumann et al, 2007):

$$\Delta\delta^i_{comb} = \sqrt{\left(\omega_H \Delta\delta^i_H\right)^2 + \left(\omega_N \Delta\delta^i_N\right)^2} \quad (1)$$

where $\Delta\delta^i_H$ and $\Delta\delta^i_N$ are ^{1}H and ^{15}N chemical-shift perturbations between OX40 mutant and WT, respectively, and $\omega_H = 1.00$ and $\omega_N = 0.15$ are normalization factors.

NMR relaxation measurements

Relaxation experiments (^{15}N T1, T2 and ^{1}H-^{15}N heteronuclear NOEs) were acquired at 800 MHz. Longitudinal (T1) and transverse (T2) relaxation data for backbone amide protons were collected using different relaxation times, T1 = 0.01, 0.59, 0.28, 0.95, 1.8, 1.34, 3, 5, 2.34, 4, 0.59, 0.95 sec and T2 = 0.01, 0.05, 0.03, 0.09, 0.07, 0.11, 0.03, 0.05 sec. R1 and R2 are commonly used to represent the inverse of T1 and T2, respectively. The ^{1}H-^{15}N heteronuclear NOEs experiments were performed using a relaxation delay of 5 sec. Data from all relaxation experiments were analyzed using CcpNmr, and data analysis was performed excluding overlapping resonances.

Intermolecular NOE mapping of lipid interactions

To determine the position of dynamic OX40-CTD in the lipid bilayer, protein-lipid distance constraints were obtained from 3D 15N-edited NOESY-TROSY-HSQC spectra recorded using 15N-labelled protein samples in bilayer liposomes composed of conventional DMPG and deuterated DH6PC ($q = 0.8$) (τNOE = 200 ms). This spectrum enables the measurement of exclusive protein-lipid NOE between the peptide chain main chain amide protons and DMPG. 2H-labelled protein samples were recorded in a bilayer lipid bilayer composed of conventional DMPG and deuterated DH6PC ($q = 0.8$), enabling the measurement of exclusive protein-lipid NOE between the peptide chain main chain amide protons and the aliphatic protons of DMPG.

 © The Author(s)

Subsequently, protein-lipid NOEs were grouped into three categories based on the position of the protein relative to the lipid. To define the position of OX40-CTD within the lipid bilayer, protein-lipid distance restraints were derived from three-dimensional ^{15}N-edited NOESY TROSY-HSQC spectra (τNOE = 200 ms) acquired with perdeuterated ^{15}N-labeled OX40-CTD reconstituted into bicelles composed of conventional DMPG and deuterated DH_6PC ($q = 0.8$). These spectra permitted the detection of intermolecular NOEs between backbone amide protons of the protein and DMPG protons.

Paramagnetic relaxation enhancement (PRE) for membrane insertion profiling

Membrane binding dynamics of OX40-CTD were probed using paramagnetic relaxation enhancement (PRE) generated by the nitroxide radical located at the terminal position of 16-doxyl stearic acid (16-DSA) (Fu et al, 2019). 16-DSA (Sigma-Aldrich) was dissolved in chloroform at concentrations of 0, 0.05, 0.1, 0.2, 0.4, 0.6, 0.8, and 1 mM. In these parallel batches, 11.2 mM DMPG and 14 mM DH_6PC were added to each of the eight samples. The mixtures were slowly dried under a nitrogen flow to form thin films, followed by overnight freeze drying. The dried films were rehydrated with phosphate buffered saline (25 mM phosphate buffered saline, pH 6.5, 100 mM NaCl) to form bilayer spheres, and 0.1 mM ^{15}N labelled OX40-CTD protein and 10% D_2O were added to adjust the final volume to 400 µL. After incubation at room temperature overnight, 2D ^{1}H-^{15}N TROSY-HSQC spectra were recorded using an 800 MHz Agilent nuclear magnetic resonance spectrometer. Residue specific PRE was calculated by comparing peak intensities in the presence (I) and absence (I_0) of 16-DSA. The residue specific PRE amplitude (PRE_{amp}) was derived by fitting the I/I_0 ratio against the 16-DSA concentration using an exponential decay model, where τ represents the decay constant. For each of the residues, we used Origin (OriginLab, Northampton, MA) to fit the PRE titration curve to exponential decay to derive the residue specific PRE amplitude (PRE_{amp}).

$$\frac{I}{I_0} = 1 - PRE_{amp}\left(1 - e^{-\frac{[16-DSA]}{\tau}}\right) \quad (2)$$

Chemical labeling of OX40-CTD with Rhodamine dye

Wild-type and mutant OX40-CTD proteins were purified to a final concentration of 0.1 mM. Proteins were fluorescently labeled with NHS Rhodamine (Thermo Scientific, 46406). Labeling reactions were carried out in 300 µL volumes containing 0.1 mM protein, 1 mM NHS-Rhodamine, and OX40 phosphate buffer, and incubated for 1 h at room temperature in the dark with gentle rotation. Following incubation, samples were dialyzed at 4 °C using 3.5 kDa molecular weight cutoff tubing against 1 L phosphate buffer for 1 h, with the dialysis repeated three times until no residual Rhodamine was detectable in the buffer. The dialyzed solution was clarified by centrifugation at 12,000 rpm for 10 min, and the supernatant was collected. Final protein concentrations were determined spectroscopically based on the absorbance ratio of Rhodamine labeled protein at 555 nm to the extinction coefficient of free Rhodamine.

For the liposome-based FRET assay, NBD-PE-containing DMPG liposomes were prepared by mixing DMPG and NBD-PE at a 10:1 molar ratio, followed by lipid film formation and rehydration in phosphate buffer. Rhodamine-labeled OX40-CTD WT or mutant proteins were incubated with the NBD-PE-containing DMPG liposomes under identical conditions. NBD-PE-containing liposomes without protein served as the negative control. Donor excitation was performed at 463 nm, and rhodamine emission was recorded at 593 nm. FRET signals were normalized to the corresponding control as indicated in the source data.

Lentiviral production for stable cell line transduction

Lentiviral supernatants encoding OX40 and its mutants were generated by co-transfecting HEK293T cells with the target plasmid together with the packaging vectors psPAX2 and pMD2.G at a 4:3:1 ratio. HEK293T cells were grown to ~70–80% confluence, the medium was replaced with 5 mL serum free DMEM, and transfection was carried out using polyethylenimine (PEI; Polysciences, USA) at a DNA:PEI ratio of 1:3. After 5 h of incubation at 37 °C with 5% CO_2, the medium was changed to fresh DMEM supplemented with 10% FBS and 1% penicillin–streptomycin. Viral supernatants were harvested 48 h later, cleared by centrifugation, and passed through a 0.45 µm filter.

For infection, HeLa cells were seeded in 10 cm dishes one day prior. When the cells reached 30–40% confluence, they were infected with viral supernatant diluted 1:1 in DMEM containing polybrene (0.8 µg/mL). After 12 h, the medium was replaced and a second round of infection was performed under the same conditions. Following another 12 h, the medium was exchanged for fresh DMEM, and cells were cultured for an additional 24 h before downstream assays.

Cell surface analysis by flow cytometry

HeLa cells were collected 24 h after infection and counted. A total of 1×10^6 cells were washed once with PBS and resuspended in 100 µL PBS. Cells were stained with anti-Flag APC antibody (1:200 dilution) for 15 min at 4 °C, followed by centrifugation at 500×*g* for 3 min and two washes with PBS. Stained cells were analyzed on a BD LSRFortessa flow cytometer using BD FACSDiva software, and data were processed with FlowJo.

Cycloheximide chase assay for protein stability

Jurkat cells stably expressing Flag-tagged OX40 WT or mutants and HuT78 sgOX40 cells reconstituted with the corresponding Flag-tagged OX40 constructs were used for cycloheximide chase assays. Cells were treated with cycloheximide (CHX; 100 µg/mL; AbMole, #M4879) to block de novo protein synthesis and harvested at the indicated time points (0, 3, 6, 9, 12, 18, 24, 48, and 60 h) to monitor protein stability. Cells were lysed on ice for 30 min in RIPA buffer (50 mM Tris-HCl pH 8.0, 150 mM NaCl, 0.1% SDS, 0.5% sodium deoxycholate, 1% Triton X-100) supplemented with protease inhibitors (ABconal, #RM02916). Lysates were clarified by centrifugation at 12,000 rpm for 15 min at 4 °C, and the supernatants were mixed with 5× loading buffer and heated at 99 °C for 10 min.

Proteins were separated by SDS-PAGE and transferred onto nitrocellulose membranes (Millipore, #HATF00010). Membranes were blocked with 5% non-fat milk in TBS-T for 1 h, washed three

© The Author(s)

times, and incubated overnight at 4 °C with mouse anti-Flag (HUABIO, #M1403-2) and mouse anti-tubulin (Sigma-Aldrich, #T5168) primary antibodies. After washing, membranes were incubated with HRP-conjugated anti-mouse secondary antibody for 1 h at room temperature. Protein bands were visualized using chemiluminescent substrate (Sigma, #WBKLS0100) and quantified with ImageJ software.

Generation of OX40 knockout HuT78 cells

OX40 knockout HuT78 cells were generated using a lentiviral CRISPR-Cas9 system. A single guide RNA targeting human OX40 was designed with the sequence 5′-GCCGGGCTTCTACAACGACG-3′ and cloned into BsmBI digested lentiCRISPR v2 using annealed oligonucleotides containing compatible overhangs. The resulting construct was transformed into DH5α competent cells, and positive clones were confirmed by Sanger sequencing with a U6 promoter primer.

Lentivirus was produced in HEK293T cells by co-transfecting the verified lentiCRISPR v2 sgOX40 plasmid with psPAX2 and pMD2.G at a 4:3:1 ratio. Viral supernatants were collected 48 h after transfection, filtered through a 0.45 μm membrane, concentrated with PEG8000 overnight at 4 °C, and pelleted by centrifugation at 4500 rpm for 40 min. The viral pellet was resuspended in IMDM supplemented with 20% FBS and 1% penicillin–streptomycin. HuT78 cells were transduced with concentrated lentivirus in the presence of 8 μg/mL polybrene. After 10–12 h, the medium was replaced with fresh IMDM containing 20% FBS and 1% penicillin–streptomycin. OX40 depletion was assessed by qPCR 24 h after transduction.

All cell lines were routinely tested and confirmed negative for mycoplasma contamination.

Reporter assay for NF-κB pathway activation

Stable reporter cell lines expressing OX40-WT or mutants, 4-1BB-WT or mutants, and CD40-WT or mutants were seeded at 2×10^4 cells per well in white 96-well plates one day before stimulation. After cell attachment, cells were treated with the corresponding ligands at serial concentrations and incubated for 18 h at 37 °C in a humidified CO_2 incubator.

NF-κB activation was assessed using the Dual-Luciferase® Reporter Assay System (Promega, #E1910). Equal volumes of Dual-Luciferase® Reagent were added to each well, mixed gently to avoid bubbles, and incubated for 15 min at room temperature in the dark. Firefly luciferase activity was then measured on a plate reader in luminescence mode with an integration time of 1 s. Subsequently, Dual-Luciferase® Stop & Glo® Reagent was added at the same volume, incubated for 10 min, and Renilla luciferase activity was recorded under identical conditions. Data were processed as follows: (1) for each sample, the firefly signal was normalized to Renilla luciferase activity; (2) the normalized ratio of the control group was used as the baseline; (3) experimental values were expressed as relative fold induction by dividing the sample ratio by the control baseline.

Immunoblotting analysis of NF-κB pathway activation

To assess the effect of TNC-scOX40L on downstream NF-κB pathway activation, Jurkat and HeLa-NF-κB + Renilla cells stably expressing OX40-WT or its mutants were seeded at 2×10^6 cells per well in six-well plates one day prior to stimulation. The following day, cells were treated with TNC-scOX40L (3.25 μg/mL) for the indicated times (0, 5, 10, 15, 30, 60, 120 min). After stimulation, cells were washed twice with ice-cold PBS and lysed in 250 μL lysis buffer containing protease inhibitors. Lysates were collected with a cell scraper into 1.5 mL tubes and disrupted by probe sonication. Supernatants were obtained by centrifugation at 12,000 rpm for 10 min at 4 °C, mixed with 3× loading buffer (2:1, v/v), and boiled at 100 °C for 15 min.

Proteins were separated by SDS-PAGE and transferred onto nitrocellulose membranes (Millipore, #HATF00010). Membranes were blocked in TBS-T with 5% non-fat milk (Sangon Biotech, #A600669) for 1 h at room temperature, washed three times, and incubated overnight at 4 °C with primary antibodies against AKT (CST, #9272), p-AKT (CST, #4060), IκBα (CST, #4812), p-IκBα (CST, #2859), p65 (CST, #8242), p-p65 (CST, #3033), and Vinculin (Merck, #V4505). The next day, membranes were washed three times with TBS-T and incubated for 1 h at room temperature with HRP-conjugated secondary antibodies (anti-mouse HRP, ABclonal, #AS003; anti-rabbit HRP, ABclonal, #AS014). Protein bands were visualized using ECL substrate (Sigma, #WBKLS0100) and quantified with ImageJ software.

Confocal co-localization analysis

Stable HeLa cell lines co-expressing OX40-GFP and TRAF2-mCherry were generated. Cells were seeded onto 35-mm glass bottom dishes at a density of 5×10^4 cells per dish and cultured overnight. Cells were stimulated with TNC-scOX40L (3.25 μg/mL) for 16 h. The following day, cells were washed twice with PBS and stained with Hoechst 33342 (Beyotime, #C1029, 1:1000 dilution) at 37 °C for 30 min. After three washes with PBS, fresh complete DMEM medium was added. Images were acquired using a Nikon AX confocal microscope equipped with a ×60 oil-immersion objective. Image processing and fluorescence intensity analyses were performed using NIS-Elements Viewer and ImageJ software.

Co-immunoprecipitation of OX40 and TRAF2

To assess the interaction between OX40 and TRAF2, HeLa-NC, HeLa-Flag-OX40, HeLa-Flag-OX40-R241S, HeLa-Flag-OX40-R242S and HeLa-Flag-OX40-2R-S cells were seeded in six-well plate at 2×10^6 cells per well. After overnight attachment, cells were either left unstimulated or stimulated with TNC-scOX40L (3.25 μg/mL) for 16 h. Cells were rinsed once with ice-cold PBS and lysed on ice using pre-chilled lysis buffer (10 mM Tris-HCl pH 7.4, 10 mM NaCl, 0.025% NP-40, 0.1 mM EDTA) supplemented with protease inhibitors, applied at 450 μl per well. Lysates were incubated on a rocker at 4 °C for 30 min, transferred to Eppendorf tubes, and briefly sonicated on ice. Clarified lysates were obtained by centrifugation at 15,000 rpm for 10 min at 4 °C.

M2 beads (5 μl per sample; Thermo Scientific, #A36798) were pre-washed three times with lysis buffer by brief centrifugation at 6000 rpm at 4 °C and kept on ice. From each clarified lysate, 45 μl of supernatant was collected as input and mixed with 15 μl of 4× SDS loading buffer before storage at −20 °C. The remaining supernatants were incubated with the pre-washed beads at 4 °C overnight on a rotator. The next day, beads were washed three times with lysis

 © The Author(s)

buffer by centrifugation at 7000 rpm at 4 °C. Bead bound proteins were eluted by adding 30 µl of 2× SDS loading buffer, and samples were stored at −20 °C until analysis. Before western blotting, samples were boiled at 100 °C for 15 min and analyzed by SDS-PAGE.

BLI assay

Bio-layer interferometry (BLI) was carried out on an Octet RED96 instrument (Sartorius) to determine the binding kinetics between TRAF2 (amino acids 310–501) and WT or 2R-S mutant forms of OX40-CTD under PG nanodisc associated conditions. All proteins were prepared in assay buffer containing 25 mM phosphate (pH 6.5), 100 mM NaCl, and 0.02% Tween-20. Purified WT, 2R-S, PIQEE-mutant, and 2R-S + PIQEE-mutant OX40-CTD proteins were pre-incubated with PG nanodiscs at room temperature before BLI measurements. Streptavidin (SSA) biosensors (Sartorius, #18-5057) were equilibrated in assay buffer for 120 s before use. Biotin labeled TRAF2 (Sangon, #C100212) was diluted to 20 ng/µL and immobilized on the SSA sensors as the ligand.

OX40-CTD samples were serially diluted in assay buffer to final concentrations of 100, 50, 25, 6.25, and 3.125 µM. Assay buffer containing the corresponding concentration of PG nanodiscs but no OX40-CTD served as the negative control. For each experiment, 200 µL of ligand and analyte solutions were dispensed into individual wells of a 96-well microplate (Molecular Devices, #5085651). Following sensor equilibration, TRAF2 was loaded onto SSA sensors for 120 s until a loading response of ~2 nm was reached. Sensors were then briefly dipped in assay buffer to establish a baseline, followed by a 300 s association step in OX40 solutions and a 300 s dissociation step in assay buffer. Sensorgrams were analyzed using Octet Analysis Studio (version 13.0.2.46). Reference subtracted curves were globally fitted to a 1:1 binding model to determine the association rate constant (k_{on}), dissociation rate constant (k_{off}), and equilibrium dissociation constant ($K_D = k_{off}/k_{on}$).

Quantitative measurement of fluorescence resonance energy transfer (FRET)

A human TRAF2 construct bearing an N-terminal mTFP tag and a GSS linker was generated and introduced into HeLa-Flag-OX40 cells and their mutants via lentiviral transduction. HeLa cells were counted and seeded at a density of 5×10^4 cells into 35-mm confocal glass-bottom dishes, followed by overnight incubation. The next day, the medium was removed, and cells were washed twice with PBS and stained with the membrane dye octadecyl rhodamine B (R18; Thermo, #0246) at 1 µM for 5 min at room temperature. After three PBS washes, cells were maintained in complete DMEM.

FRET efficiency between mTFP (donor) and R18 (acceptor) was measured on a Zeiss LSM 900 confocal microscope using the acceptor photobleaching method. mTFP was excited at 458 nm and emission was collected at 470–550 nm, whereas R18 was excited at 561 nm and emission was detected at 570–650 nm. Complete photobleaching of R18 was achieved by applying the 561 nm laser at 100% intensity for 60 s across the whole cell. mTFP fluorescence was recorded three times before and after bleaching. FRET efficiency was calculated using the formula:

$$FRET_{eff} = \frac{FL_{AP} - FL_{BP}}{FL_{AP}} \quad (3)$$

where FL_{AP} and FL_{BP} represent mTFP fluorescence after and before R18 photobleaching, respectively.

For quantitative analysis, individual cells with detectable mTFP-TRAF2 fluorescence and clear R18 membrane labeling were analyzed. Each data point represents the FRET efficiency measured from one individual cell. Measurements were performed in three independent biological experiments, and the total number of cells analyzed for each construct is indicated in the corresponding figure legend.

Recombinant TNF ligands and stimulation conditions

The extracellular domain of human OX40L (residues 51–183) was cloned as three tandem protomer domains connected by peptide linkers into a pcDNA3.1(+) expression vector containing a C-terminal His tag (Table 1). A tenascin-C (TNC) trimerization domain was fused at the N-terminus to promote spontaneous oligomerization of the ligand into higher-order assemblies, thereby enhancing receptor clustering and signaling activation.

Recombinant ligands were expressed in Expi293F cells. Prior to transfection, cells were adjusted to a density of $3–5 \times 10^6$ cells/mL in fresh medium. Plasmid DNA and polyethyleneimine (PEI) were pre-incubated to form DNA-PEI complexes. For a 20 mL culture, 26 µg plasmid DNA (1.3 mg/L) was diluted in 1 mL culture medium and mixed with PEI. The PEI-DNA complexes were added dropwise to the cell culture with gentle swirling to ensure even distribution. The day of transfection was designated as Day 0, and cells were maintained at 37 °C with shaking.

Approximately 24 h post-transfection, 6% feed medium (Unionbiotech, Cat# UF1003) was added. Four days after transfection, cells were harvested by centrifugation at 4500 rpm for 15 min, and the supernatant was collected. The supernatant was incubated with Ni-NTA beads at 4 °C for 1 h. After binding, beads were washed with buffer (20 mM HEPES, 150 mM NaCl, pH 7.4), followed by washing with buffer containing 20 mM imidazole to remove non-specifically bound proteins. The target protein was eluted using buffer containing 300 mM imidazole. Eluted fractions were further purified by size-exclusion chromatography using a Superdex 200 column. Fractions corresponding to properly assembled ligand were pooled, concentrated, quantified, and used for subsequent signaling assays.

TNC-scOX40L:

MRAWIFFLLSLAGRALAAPLAACGCAAAPDIKDLLSRLEELE
GLVSSLREQQVSHRYPRIQSIKVQFTEYKKEKGFILTSQKEDEIM
KVQNNSVIINCDGFYLISLKGYFSQEVNISLHYQKDEEPLFQLK
KVRSVNSLMVASLTYKDKVYLNVTTDNTSLDDFHVNGGELILI
HQNPGEFCVLGSGGSGQVSHRYPRIQSIKVQFTEYKKEKGFILT
SQKEDEIMKVQNNSVIINCDGFYLISLKGYFSQEVNISLHYQKD
EEPLFQLKKVRSVNSLMVASLTYKDKVYLNVTTDNTSLDDFH
VNGGELILIHQNPGEFCVLGSGGSGQVSHRYPRIQSIKVQFTEY
KKEKGFILTSQKEDEIMKVQNNSVIINCDGFYLISLKGYFSQEV-
NISLHYQKDEEPLFQLKKVRSVNSLMVASLTYKDKVYLNVTTD
NTSLDDFHVNGGELILIHQNPGEFCVLHHHHHH.

© The Author(s)

Preparation and reconstitution of PG nanodiscs

1,2-Dimyristoyl-sn-glycero-3-phosphoglycerol (DMPG) was dissolved in chloroform, dried under a stream of nitrogen to form a thin lipid film, and further vacuum-dried to remove residual solvent. The lipid film was rehydrated and solubilized in buffer containing sodium deoxycholate. Solubilized DMPG was mixed with membrane scaffold protein MSP1D1 at a molar ratio of 80:1 (DMPG:MSP1D1) and incubated at room temperature for 1 h. Detergent removal was achieved by dialysis at room temperature against buffer identical to that used for protein experiments. Following dialysis, samples were clarified by high-speed centrifugation and purified by size-exclusion chromatography using FPLC. Nanodisc-containing fractions were collected and quantified.

For reconstitution, purified OX40-CTD was mixed with PG nanodiscs and incubated at room temperature for 15 min prior to NMR measurements.

Statistical analysis

Statistical analyses were performed using GraphPad Prism software. Data are presented as mean ± SD unless otherwise indicated in the figure legends. The number of independent biological replicates, independent protein preparations, or analyzed cells is indicated in the corresponding figure legends. For comparisons between two groups, independent samples *t* tests, also referred to as unpaired two-tailed Student's *t* tests were used. For comparisons among more than two groups with a single control group, ordinary one-way ANOVA followed by Dunnett's multiple comparisons test was used. For experiments involving two independent variables, including CHX chase assays, ordinary two-way ANOVA followed by Dunnett's multiple comparisons test was used to compare each experimental group with the corresponding WT or control group across the indicated time points. For dose–response reporter assays, EC_{50} values were generated by nonlinear regression using a four-parameter logistic model; statistical comparisons between WT and mutant receptors were performed at the indicated ligand concentrations using the tests specified in the corresponding figure legends. Exact or adjusted *P* values are provided in the corresponding figure legends. *P* values less than 0.05 were considered statistically significant. Significance was denoted as follows: ns, not significant; $^{*}P < 0.05$; $^{**}P < 0.01$; $^{***}P < 0.001$; $^{****}P < 0.0001$.

Data availability

Correspondence and requests for materials should be addressed to Prof. Linlin Zhao (lzhao@tongji.edu.cn). All unique reagents and constructs generated in this study are available from the corresponding author upon reasonable request and completion of a material transfer agreement, if required. All data supporting the findings of this study are available within the article and its Appendix files. Source data for the main figures are provided as figure-specific source data files, and source data for Appendix figures are provided as a combined Appendix source data archive. No custom code was used in this study.

The source data of this paper are collected in the following database record: biostudies:S-SCDT-10_1038-S44318-026-00868-z.

Expanded view data, supplementary information, appendices are available for this paper at https://doi.org/10.1038/s44318-026-00868-z.

Peer review information

A peer review file is available at https://doi.org/10.1038/s44318-026-00868-z

References

Bartels C, Xia TH, Billeter M, Guntert P, Wuthrich K (1995) The program XEASY for computer-supported NMR spectral analysis of biological macromolecules. J Biomol NMR 6:1–10

Ceccarelli A, Di Venere A, Nicolai E, De Luca A, Rosato N, Gratton E, Mei G, Caccuri AM (2017) New insight into the interaction of TRAF2 C-terminal domain with lipid raft microdomains. Biochim Biophys Acta Mol Cell Biol Lipids 1862:813–822

Chen L, Flies DB (2013) Molecular mechanisms of T cell co-stimulation and co-inhibition. Nat Rev Immunol 13:227–242

Compaan DM, Hymowitz SG (2006) The crystal structure of the costimulatory OX40-OX40L complex. Structure 14:1321–1330

Croft M (2003) Co-stimulatory members of the TNFR family: keys to effective T-cell immunity? Nat Rev Immunol 3:609–620

Croft M (2009) The role of TNF superfamily members in T-cell function and diseases. Nat Rev Immunol 9:271–285

Croft M (2010) Control of immunity by the TNFR-related molecule OX40 (CD134). Annu Rev Immunol 28:57–78

Delaglio F, Grzesiek S, Vuister GW, Zhu G, Pfeifer J, Bax A (1995) NMRPipe: a multidimensional spectral processing system based on UNIX pipes. J Biomol NMR 6:277–293

Edner NM, Carlesso G, Rush JS, Walker LSK (2020) Targeting co-stimulatory molecules in autoimmune disease. Nat Rev Drug Discov 19:860–883

Fu Q, Piai A, Chen W, Xia K, Chou JJ (2019) Structure determination protocol for transmembrane domain oligomers. Nat Protoc 14:2483–2520

Harayama T, Riezman H (2018) Understanding the diversity of membrane lipid composition. Nat Rev Mol Cell Biol 19:281–296

Jaeger-Ruckstuhl CA, Lo Y, Fulton E, Waltner OG, Shabaneh TB, Simon S, Muthuraman PV, Correnti CE, Newsom OJ, Engstrom IA et al (2024) Signaling via a CD27-TRAF2-SHP-1 axis during naive T cell activation promotes memory-associated gene regulatory networks. Immunity 57:287–302.e212

Jiang Y, Dai A, Huang Y, Li H, Cui J, Yang H, Si L, Jiao T, Ren Z, Zhang Z et al (2025) Ligand-induced ubiquitination unleashes LAG3 immune checkpoint function by hindering membrane sequestration of signaling motifs. Cell 188:2354–2371.e2318

Katsarou A, Sjostrand M, Naik J, Mansilla-Soto J, Kefala D, Kladis G, Nianias A, Ruiter R, Poels R, Sarkar I et al (2021) Combining a CAR and a chimeric costimulatory receptor enhances T cell sensitivity to low antigen density and promotes persistence. Sci Transl Med 13:eabh1962

Kawamata S, Hori T, Imura A, Takaori-Kondo A, Uchiyama T (1998) Activation of OX40 signal transduction pathways leads to tumor necrosis factor receptor-associated factor (TRAF) 2- and TRAF5-mediated NF-kappaB activation. J Biol Chem 273:5808–5814

Kay LE, Ikura M, Tschudin R, Bax A (2011) Three-dimensional triple-resonance NMR Spectroscopy of isotopically enriched proteins. 1990. J Magn Reson 213:423–441

Larson RC, Maus MV (2021) Recent advances and discoveries in the mechanisms and functions of CAR T cells. Nat Rev Cancer 21:145–161

Mackensen A, Muller F, Mougiakakos D, Boltz S, Wilhelm A, Aigner M, Volkl S, Simon D, Kleyer A, Munoz L et al (2022) Anti-CD19 CAR T cell therapy for refractory systemic lupus erythematosus. Nat Med 28:2124–2132

 © The Author(s)

Matsuzawa A, Tseng PH, Vallabhapurapu S, Luo JL, Zhang W, Wang H, Vignali DA, Gallagher E, Karin M (2008) Essential cytoplasmic translocation of a cytokine receptor-assembled signaling complex. Science 321:663–668

McWhirter SM, Pullen SS, Holton JM, Crute JJ, Kehry MR, Alber T (1999) Crystallographic analysis of CD40 recognition and signaling by human TRAF2. Proc Natl Acad Sci USA 96:8408–8413

Morris GP, Allen PM (2012) How the TCR balances sensitivity and specificity for the recognition of self and pathogens. Nat Immunol 13:121–128

Rauert H, Stuhmer T, Bargou R, Wajant H, Siegmund D (2011) TNFR1 and TNFR2 regulate the extrinsic apoptotic pathway in myeloma cells by multiple mechanisms. Cell Death Dis 2:e194

Rauert H, Wicovsky A, Muller N, Siegmund D, Spindler V, Waschke J, Kneitz C, Wajant H (2010) Membrane tumor necrosis factor (TNF) induces p100 processing via TNF receptor-2 (TNFR2). J Biol Chem 285:7394–7404

Renand A, Cervera-Marzal I, Gil L, Dong C, Garcia A, Kervagoret E, Auble H, Habes S, Chevalier C, Vavasseur F et al (2020) Integrative molecular profiling of autoreactive CD4 T cells in autoimmune hepatitis. J Hepatol 73:1379–1390

Salzmann M, Wider G, Pervushin K, Wuthrich K (1999) Improved sensitivity and coherence selection for [15N,1H]-TROSY elements in triple resonance experiments. J Biomol NMR 15:181–184

Schumann FH, Riepl H, Maurer T, Gronwald W, Neidig KP, Kalbitzer HR (2007) Combined chemical shift changes and amino acid specific chemical shift mapping of protein-protein interactions. J Biomol NMR 39:275–289

Singh PK, Rybak JA, Schuck RJ, Sahoo AR, Buck M, Barrera FN, Smith AW (2024) Phosphatidylinositol 4,5-bisphosphate drives the formation of EGFR and EphA2 complexes. Sci Adv 10:eadl0649

Skotland T, Sandvig K (2019) The role of PS 18:0/18:1 in membrane function. Nat Commun 10:2752

So T, Choi H, Croft M (2011) OX40 complexes with phosphoinositide 3-kinase and protein kinase B (PKB) to augment TCR-dependent PKB signaling. J Immunol 186:3547–3555

Song J, So T, Cheng M, Tang X, Croft M (2005) Sustained survivin expression from OX40 costimulatory signals drives T cell clonal expansion. Immunity 22:621–631

Tan J, Jia Y, Zhou M, Fu C, Tuhin IJ, Ye J, Monty MA, Xu N, Kang L, Li M et al (2022) Chimeric antigen receptors containing the OX40 signalling domain enhance the persistence of T cells even under repeated stimulation with multiple myeloma target cells. J Hematol Oncol 15:39

Thapa B, Kato S, Nishizaki D, Miyashita H, Lee S, Nesline MK, Previs RA, Conroy JM, DePietro P, Pabla S et al (2024) OX40/OX40 ligand and its role in precision immune oncology. Cancer Metastasis Rev 43:1001–1013

Vranken WF, Boucher W, Stevens TJ, Fogh RH, Pajon A, Llinas M, Ulrich EL, Markley JL, Ionides J, Laue ED (2005) The CCPN data model for NMR spectroscopy: development of a software pipeline. Proteins 59:687–696

Wang T, Yang Y, Ma L, Feng R, Li J, Zhang C, Bai J, Ding Y, Liu G, Wu F et al (2024) BCMA-BBZ-OX40 CAR-T therapy using an instant manufacturing platform in multiple myeloma. J Immunother Cancer 12:e009476

Wang Y, Gao J, Guo X, Tong T, Shi X, Li L, Qi M, Wang Y, Cai M, Jiang J et al (2014) Regulation of EGFR nanocluster formation by ionic protein-lipid interaction. Cell Res 24:959–976

Wehrli M, Maus MV (2021) New CARs on and off the road: challenges and new developments in CAR-T cell therapy. Curr Opin Pharm 59:116–126

Wen M, Cao Y, Wu B, Xiao T, Cao R, Wang Q, Liu X, Xue H, Yu Y, Lin J et al (2021) PD-L1 degradation is regulated by electrostatic membrane association of its cytoplasmic domain. Nat Commun 12:5106

Xiao X, Balasubramanian S, Liu W, Chu X, Wang H, Taparowsky EJ, Fu YX, Choi Y, Walsh MC, Li XC (2012) OX40 signaling favors the induction of T(H)9 cells and airway inflammation. Nat Immunol 13:981–990

Xu C, Gagnon E, Call ME, Schnell JR, Schwieters CD, Carman CV, Chou JJ, Wucherpfennig KW (2008) Regulation of T cell receptor activation by dynamic membrane binding of the CD3epsilon cytoplasmic tyrosine-based motif. Cell 135:702–713

Yang W, Pan W, Chen S, Trendel N, Jiang S, Xiao F, Xue M, Wu W, Peng Z, Li X et al (2017) Dynamic regulation of CD28 conformation and signaling by charged lipids and ions. Nat Struct Mol Biol 24:1081–1092

Ye H, Park YC, Kreishman M, Kieff E, Wu H (1999) The structural basis for the recognition of diverse receptor sequences by TRAF2. Mol Cell 4:321–330

Ye H, Wu H (2000) Thermodynamic characterization of the interaction between TRAF2 and tumor necrosis factor receptor peptides by isothermal titration calorimetry. Proc Natl Acad Sci USA 97:8961–8966

Yen HY, Hoi KK, Liko I, Hedger G, Horrell MR, Song W, Wu D, Heine P, Warne T, Lee Y et al (2018) PtdIns(4,5)P(2) stabilizes active states of GPCRs and enhances selectivity of G-protein coupling. Nature 559:423–427

Zhang H, Li F, Cao J, Wang X, Cheng H, Qi K, Wang G, Xu K, Zheng J, Fu YX et al (2021) A chimeric antigen receptor with antigen-independent OX40 signaling mediates potent antitumor activity. Sci Transl Med 13:eaba7308

Zhang H, Zhong R, Wang W, Huang Y, Li F, Liang J, Zhang J, Yu Z, Zhong H, Lu S et al (2025) OX40-heparan sulfate binding facilitates CAR T cell penetration into solid tumors in mice. Sci Transl Med 17:eadr2151

Acknowledgements

We thank the staff members of the Nuclear Magnetic Resonance System (https://cstr.cn/31129.02.NFPS.NMRSystem) at the National Facility for Protein Science in Shanghai (https://cstr.cn/31129.02.NFPS) for providing technical support and assistance in data collection and analysis. This work was supported by the National Natural Science Foundation of China (32301027, 32571410 to LZ; 82350710799 to JC and LZ), the Shanghai Health Commission Clinical Research Special Youth Project (2022YQ079 to LZ), the Science and Technology Commission of Shanghai Municipality (22JC1410500 to JC), the Strategic Priority Research Program of the Chinese Academy of Sciences (XDB1060000 to JC), and the Shanghai Basic Research Pioneer Project and the Shanghai Municipal Science and Technology Major Project (both to JC).

Author contributions

Jiali Zhu: Conceptualization; Resources; Software; Investigation. **Xi Xu**: Investigation. **Pei Liu**: Validation; Investigation. **Hui Wu**: Investigation. **Yuxuan Wang**: Investigation. **Boying Xu**: Investigation. **Maorong Wen**: Resources. **Min Chen**: Investigation. **Zhifeng Chen**: Resources; Supervision; Investigation; Writing—review and editing. **James J Chou**: Conceptualization; Resources; Visualization; Writing—review and editing. **Linlin Zhao**: Conceptualization; Resources; Data curation; Investigation; Writing—original draft; Writing—review and editing.

Source data underlying figure panels in this paper may have individual authorship assigned. Where available, figure panel/source data authorship is listed in the following database record: biostudies:S-SCDT-10_1038-S44318-026-00868-z.

Disclosure and competing interests statement

The authors declare no competing interests.

Open Access This article is licensed under a Creative Commons Attribution 4.0 International License, which permits use, sharing, adaptation, distribution and reproduction in any medium or format, as long as you give appropriate credit to the original author(s) and the source, provide a link to the Creative Commons licence, and indicate if changes were made. The images or other third party material in this article are included in the article's Creative Commons licence, unless indicated otherwise in a credit line to the material. If material is not

included in the article's Creative Commons licence and your intended use is not permitted by statutory regulation or exceeds the permitted use, you will need to obtain permission directly from the copyright holder. To view a copy of this licence, visit http://creativecommons.org/licenses/by/4.0/. Creative Commons Public Domain Dedication waiver http://creativecommons.org/publicdomain/zero/1.0/ applies to the data associated with this article, unless otherwise stated in a credit line to the data, but does not extend to the graphical or creative elements of illustrations, charts, or figures. This waiver removes legal barriers to the re-use and mining of research data. According to standard scholarly practice, it is recommended to provide appropriate citation and attribution whenever technically possible.

© The Author(s) 2026, modified publication 2026